Chemie der Erde 77 (2017) 517–533

Contents lists available at ScienceDirect

Chemie der Erde

journal homepage: www.elsevier.de/chemer

Geochemistry and petrogenesis of the Eocene back arc mafic rocks in the Zagros suture zone, northern Noorabad, western Iran

Fatemeh Nouri[a,*], Yoshihiro Asahara[b], Hossein Azizi[c], Koshi Yamamoto[b], Motohiro Tsuboi[d]

[a] Geology Department, Faculty of Basic Sciences, Tarbiat Modares University, Tehran, Iran
[b] Department of Earth and Environmental Sciences, Graduate School of Environmental Studies, Nagoya University, Nagoya 464-8601, Japan
[c] Mining Department, Faculty of Engineering, University of Kurdistan, Sanandaj, Iran
[d] Department of Applied Chemistry for Environment, School of Science and Technology, Kwansei Gakuin University, Sanda 669-1337, Japan

ARTICLE INFO

Article history:
Received 5 February 2017
Received in revised form 6 June 2017
Accepted 12 June 2017
Editorial handling - Hadi Shafaii Moghadam

Keywords:
Zagros orogeny
Neo-Tethys
Extensional basin
Metasomatized mantle
Sr-Nd isotope ratios

ABSTRACT

The northern Noorabad area in western Iran contains several gabbro and basalt bodies which were emplaced along the Zagros suture zone. The basalts show pillow and flow structures with amygdaloidal textures, and the gabbroic rocks show massive and foliated structures with coarse to fine-grained textures. The SiO_2 contents of the gabbros and basalts are similar and range from 46.1–51.0 wt.%, and the Al_2O_3 contents vary from 12.3–18.8 wt.%, with TiO_2 contents of 0.4–3.0 wt.%. The Nb concentrations of some gabbros and basalts are high and can be classified as Nb-enriched arc basalts. The positive εNd(t) values (+3.7 to +9.8) and low $^{87}Sr/^{86}Sr_{(initial)}$ ratios (0.7031–0.7071) of both bodies strongly indicate a depleted mantle source and indicate that the rocks were formed by partial melting of a depleted lithospheric mantle and interaction with slab fluids/melts. The chemical composition of trace elements, REE pattern and initial $^{87}Sr/^{86}Sr$-$^{143}Nd/^{144}Nd$ ratios show that the rocks have affinities to tholeiitic magmatic series and suggest an extensional tectonic regime over the subduction zone for the evolution of these rocks. We propose an extensional tectonic regime due to the upwelling of metasomatized mantle after the late Cretaceous collision in the Harsin-Noorabad area. These rocks can be also considered as Eocene back arc magmatic activity along the Zagros suture zone in this area.

© 2017 Elsevier GmbH. All rights reserved.

1. Introduction

The Iranian plateau is a tectonically active region within the Alpine-Himalayan orogenic belt. It contains a number of continental fragments that have been welded together along a suture zone of oceanic character from the Early Paleozoic to Late Tertiary. Stöcklin and Nabavi (1972) divided the Iranian plateau into eight segments (Fig. 1) including Zagros fold-thrust belt, Sanandaj-Sirjan, Urmia-Dokhtar magmatic arc, central Iran, Alborz, Kopeh Dagh and eastern Iran. Amongst the microcontinents, some oceanic crust and island arc such as Proto-Tethys, Paleo-Tethys and Neo-Tethys are preserved. The main remnant of the Neo-Tethys oceanic crust is Zagros ophiolite that is developed in the Zagros suture zone in the west of Iran and southern part of Turkey (Şengör, 1987; Alavi, 1994; Azizi and Moinevaziri, 2009; Paul et al., 2010; Wrobel Daveau et al., 2010; Azizi et al., 2011a,b; Azizi et al., 2013; Saccani et al., 2013; Whitechurch et al., 2013; Shafaii Moghadam and Stern, 2015). In the last three decades, many researchers have been interested in the Zagros suture zone (Buday, 1980; Delaloye and Desmons, 1980; Desmons and Beccaluva, 1983; Ghazi and Hassanipak, 1999; Alavi, 2004; Shafaii Moghadam et al., 2009; Allahyari et al., 2010; Shafaii Moghadam and Stern, 2011; Ali et al., 2013; Ali and Aswad, 2013; Saccani et al., 2013; Whitechurch et al., 2013; Azizi et al., 2013; Allahyari et al., 2014; Aswad et al., 2014; Saccani et al., 2014; Ao et al., 2016; Shafaii Moghadam and Stern, 2015; Nouri et al., 2016) and have suggested various tectonic regimes for some parts on the ophiolites in the Zagros orogeny such as supra-subduction origin, plume, MORB sources, oceanic island basalt (OIB) and island arc to back arc tectonic settings. Although many studies have examined the magmatic activity of the Zagros orogenic belt in western Iran, no detailed information has been reported on the Harsin dismembered ophiolite in the Zagros Mountains prior and during the collision of the Arabian and Iranian Plates.

In the Zagros suture zone, the Biston-Avoraman block (BAVB), which is similar to the Arabian plate and probably contains Precambrian basement (Şengör, 1987; Jassim and Goff, 2006; Okay et al.,

* Corresponding author.
E-mail address: F.nourisandiani@gmail.com (F. Nouri).

http://dx.doi.org/10.1016/j.chemer.2017.06.002
0009-2819/© 2017 Elsevier GmbH. All rights reserved.

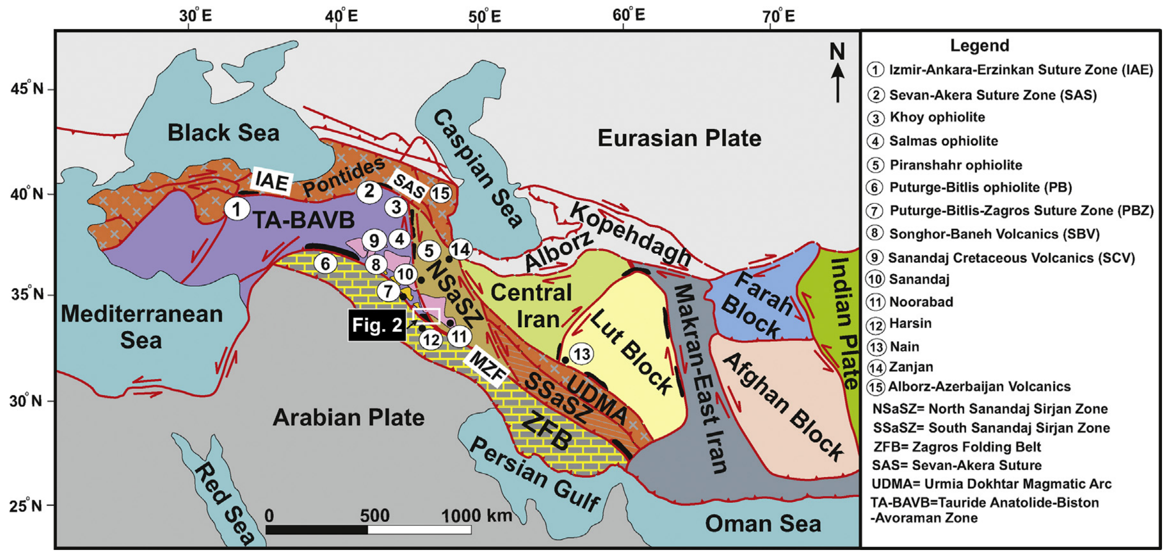

Fig. 1. Simplified geological map of the eastern Turkey and Iranian Plateau (modified from Nouri et al., 2016).

2008; Azizi et al., 2013), is squeezed between the Sanandaj-Sirjan zone in the east (Azizi and Moinevaziri, 2009; Azizi et al., 2011a,b; Azizi et al., 2015a,b; Azizi et al., 2016) and Arabian Plate in the west (Fig. 1). The BAVB now underlies a tall cliff in the Kermanshah area referred to as Biston Mountains. Several researchers concluded that thick limestone sequences were deposited in Arabian passive margin on an epi-continental basement (Ricou et al., 1977; Braud, 1978; Kazmin et al., 1986; Stampfli et al., 1991; Pillevuit et al., 1997; Shahidi and Nazari, 1997; Karimi Bavandpur and Hajihoseini, 1999; Mohajjel et al., 2003; Vergés et al., 2011). Jassim and Goff (2006) concluded that the BAVB, TA (Tauride Anatolide) and Hawasina blocks were a fragment of Arabian Plate in the Neo-Tethys Ocean. In addition, Wrobel Daveau et al. (2010) regarded the BAVB as fragment of the Arabian Plate that was squeezed between the Iranian and Arabian Plates and suggested that an upwelling mantle plume had a major role in separating the BAVB from the Arabian Plate. The same scenario was suggested by Azizi et al. (2013) and Nouri et al. (2016). Detailed discussion of the geodynamic of the BAVB by Jassim and Goff (2006) was based on the assumption that the BAVB underwent the same evolution as the TA block in southern Turkey and the Hawasina block in Oman. Given this situation, correlation between the TA block and the BAVB will clear up the relationships among the BAVB, TA block and Arabian Plate.

In addition, the TA block initially belonged to the Arabian Plate but separated from this continent during the Triassic Era (Okay, 2008). Monod et al. (2003) reported Ordovician glacial deposits in the TA block overlain by a huge volume of Mesozoic carbonate rocks (Okay, 2008). The radiometric dating of the TA basement yielded an age of 550 Ma (Okay et al., 2002). To the south, in the Biston area along the Iran-Iraq border, the basement is not exposed and is perhaps hidden under a large volume of Triassic-Jurassic carbonate deposits. Good correlation of Triassic and younger sedimentary rocks in the Biston area with those in the TA block lead us to believe that this zone is a segment of the Arabian Plate even without a report of Precambrian basement similar to that of the TA block in southern Turkey.

The Zagros ophiolite in the west of Iran and southern Turkey has been separated by the Tauride Anatolide – Biston Avoraman micro-continental block (Fig. 1). The Izmir-Ankara-Erzinkan suture zone (IAE) (Okay and Tüysüz, 1999) or the Northern Neo-Tethys remnant (Şengör and Yilmaz, 1981) is a junction between the Eurasian Plate and Tauride Anatolide block (Fig. 1). The south suture zone, which is situated between the Arabian Plate in the south and the Tauride Anatolide block in the north, is known as the Pütürge–Bitlis–Zagros (PBZ) suture zone (Okay and Tüysüz, 1999; Yilmaz and Özel, 2008). Recent reports by Azizi et al. (2013) and Nouri et al. (2016) have designated two parallel ophiolite zones in the Kermanshah–Harsin area which match with the IAE and PBZ suture zones in the northern and southern Tauride Anatolide block in Turkey, respectively (Fig. 1).

In this study, we report new geochemical and isotopic data from the Harsin-Noorabad mafic bodies, which have been considered to be part of the Cretaceous ophiolite before this study (Ghazi and Hassanipak, 1999; Allahyari et al., 2012; Saccani et al., 2013; Kiani et al., 2015; Tahmasbi et al., 2016). The petrogenesis and tectonic setting of these rocks are poorly constrained because geochemical and isotopic data remain scarce and only regional studies have been carried out on the area under investigation (Shahidi and Nazari, 1997). We discuss the significance and implication of these data in describing the heterogeneous lithology and geological makeup of the Neo-Tethys oceanic crust that is exposed in the Zagros suture zone. In this paper, we focus on the earlier suture zone and development of back arc magmatism in the Eocene after Late Cretaceous collision between Arabian Plate and BAVB block. Then, we show the connection of these rocks to the extensional tectonic regime over the subduction such as a back arc basin tectonic regime.

2. Regional geology and field relations

The Harsin-Noorabad area is situated in western Iran along the Zagros suture zone. The oldest rocks are Biston sedimentary rocks (Fig. 2) which were epi-continental facies (Shahidi and Nazari, 1997) and were thrusted over Cretaceous or younger unites.

Cretaceous ophiolite mélange is a main component of the igneous bodies and includes ultramafic, gabbro and rarely basaltic rocks (Fig. 2). Clear separation of the rocks is difficult because they are deformed and mixed with sediments. In most part, dynamic deformations have affected the entire ophiolite complex which occur as irregular blocks or bands within Eocene and Miocene unites. The ophiolite complex occurs as tectonic slices in fault contact with Eocene complex and thrusted over Quaternary deposit due to young activities of Zagros fault (Fig. 2). Allahyari et al. (2010) suggested that these rocks were formed in the middle oceanic ridge with tholeiitic composition.

The Eocene mafic-sedimentary complex (Fig. 2) is the focus of this paper and is mostly different from Cretaceous ophiolite.

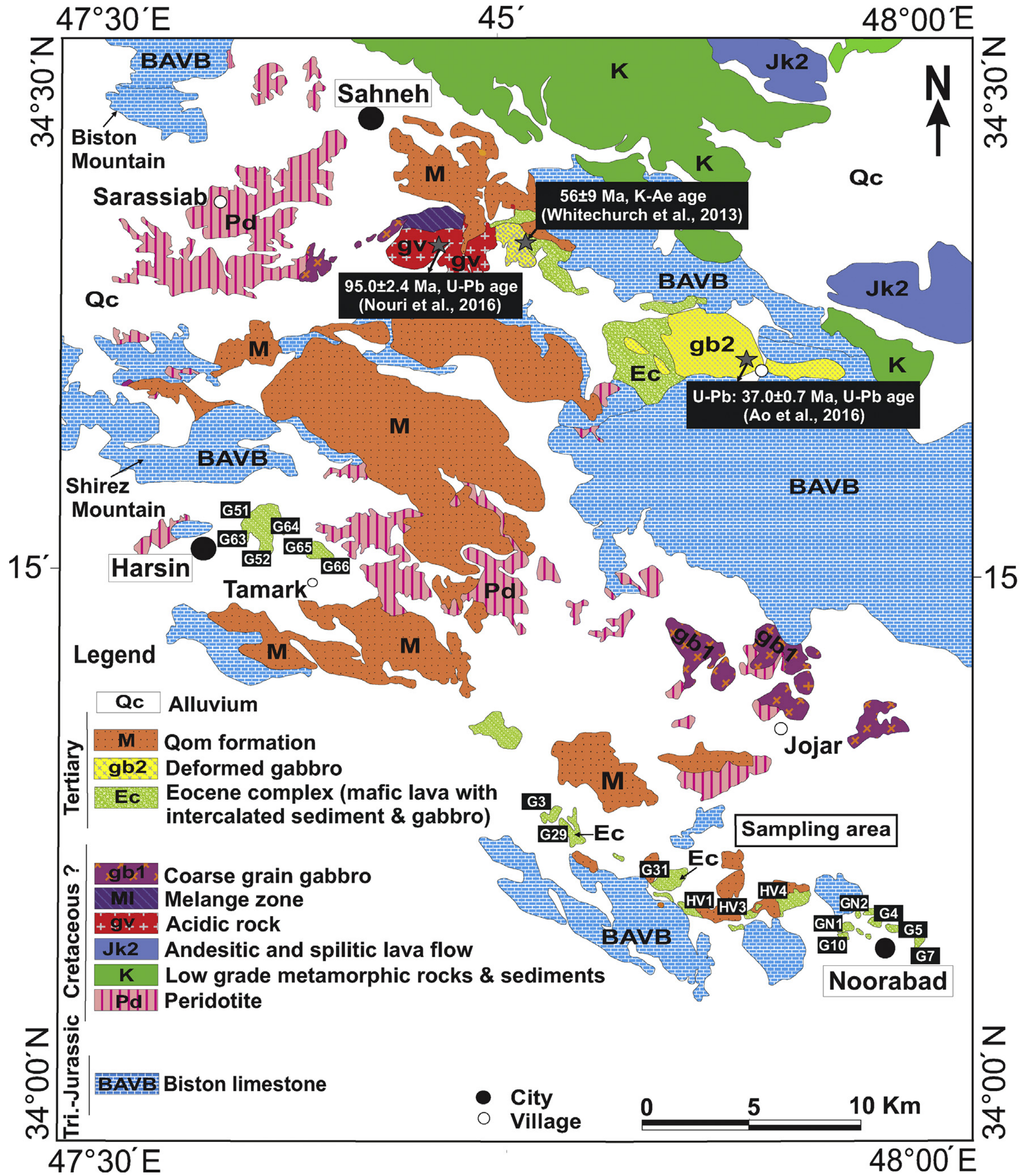

Fig. 2. Geological map of the Harsin area modified after the geological map of Shahidi and Nazari (1997).

The relationship of the complex with Cretaceous ophiolite is not clear and in some parts cut the Cretaceous complex. The main component in the Eocene complex includes limestone, shale and sandstone with mafic volcanic and plutonic rocks. Braud (1978) and Shahidi and Nazari (1997) suggested that this complex was formed in the Early to Middle Eocene (fossils such as Nummulites sp., Lockarita cf. conditi, Alveolina cf. elongate, Orbitolites sp. Globorotalia spinulosa and so on) based on stratigraphic relationship.

In this complex, gabbros are fine to coarse grained and locally show layering, and the bodies are more deformed and mainly altered near the Noorabad area (Fig. 3a). Mylonitic foliation is developed in the western part of the body, and in some places they are converted to Mylonitic gabbro. They have been metamorphosed at green schist facies and contain chlorite and secondary epidote. They have been mapped as Eocene complex in the Harsin geological map (Braud, 1978; Shahidi and Nazari, 1997). Whitechurch et al. (2013) suggested arc to back arc tectonic regimes for Eocene mafic complex in this area. They determined Eocene age for these gabbros based on K-Ar and U-Pb dating (Whitechurch et al., 2013; Ao et al., 2016) in the northern Harsin. In some part, the carbonate beds overlie the gabbros (Fig. 3b). Toward the east, most parts is coarse grained gabbros and the gabbro bodies are present as massive layers (Fig. 3c), lenses and boudins in the Eocene sediments. It is not clear if the mafic rocks represent intrusive sills or alternatively allochtonous imbricates of mafic rocks within the Eocene sediments. Above the lenses of some gabbros, mafic flows intrude into the carbonate matrix, leading to recrystallization of carbonate slices (Fig. 3d).

The volcanic sequence includes basaltic rocks with interbedded carbonate and shale (Fig. 3e). The mafic lava occurs as massive flow

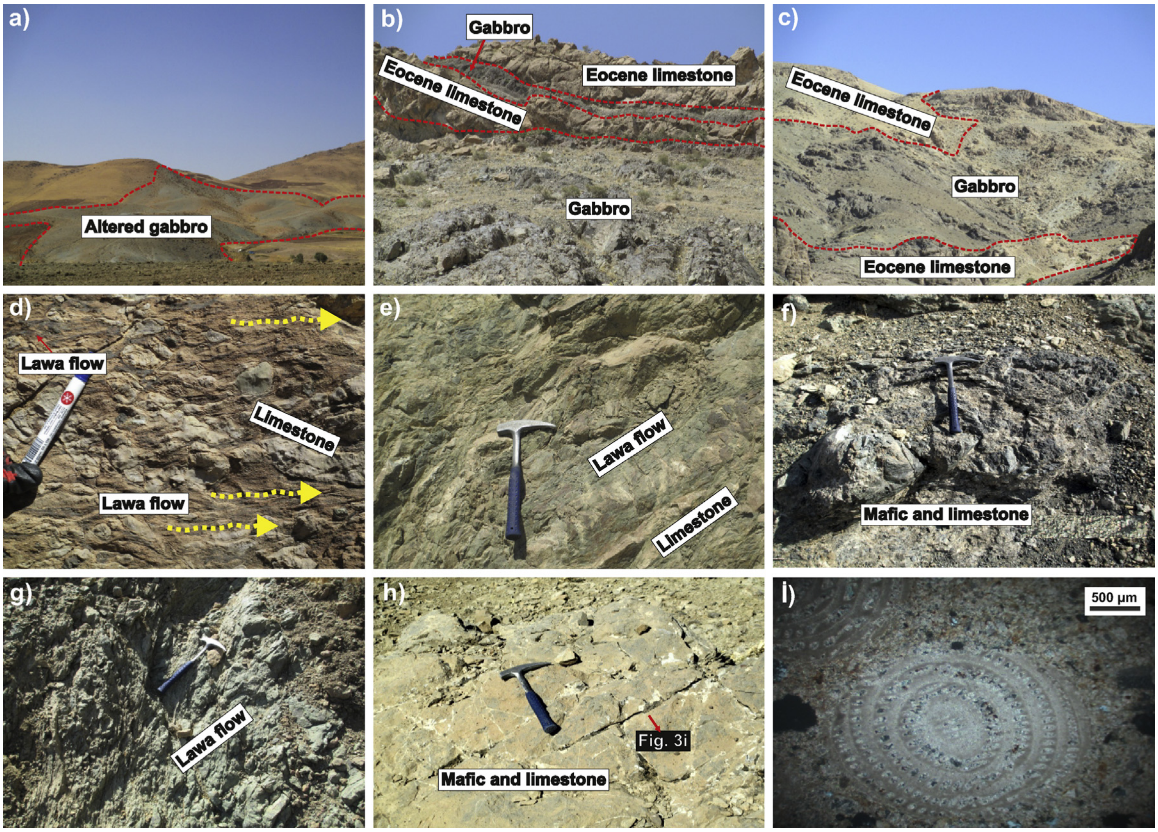

Fig. 3. (a) Noorabad gabbro outcrops. (b) The carbonate bed overlie the gabbro. (c) The gabbro body is present as massive layer in the Eocene sediments. (d) Mafic lava flows intrude into the carbonate matrix, leading to recrystallization of carbonate slices. (e) The volcanic sequence includes basaltic rocks with intercalated carbonate and shale. (f, g) The mafic lava occurs as massive flow and pillow. (h) The volcano-sediment succession with fragmented features. (i) The Nummulites fossil in the sediments with Eocene age.

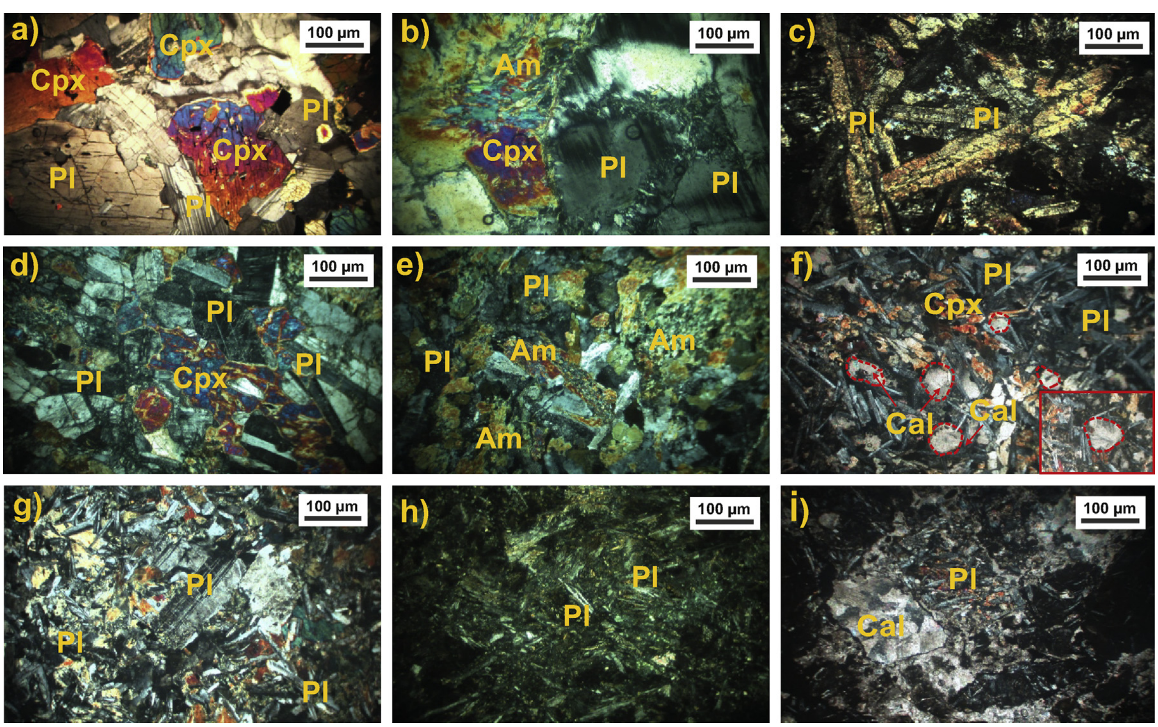

Fig. 4. Photomicrographs of the Harsin-Noorabad mafic rocks. (a, b) Granular, micro granular textures in the gabbroic rocks. (c, d) Plagioclase and pyroxene in the gabbros. The plagioclase crystals are euhedral to subhedral, and the pyroxenes generally exhibit clear cleavage traces and are subhedral phenocrysts. (e) Uralitization and sasussritization in altered sample. (f, g) Plagioclase and clinopyroxene fine-grain groundmass with occasional plagioclase microphenocryst in the basalts. (h) The plagioclase grains with irregular borders and skeletal shape. (i) Plagioclase and pyroxene assemblages in the calcite groundmass. Most of the plagioclases and pyroxenes are broken and crushed in peperites. Symbols: Pl = plagioclase; Cpx = clinopyroxene; Am = amphibole; Cal = calcite.

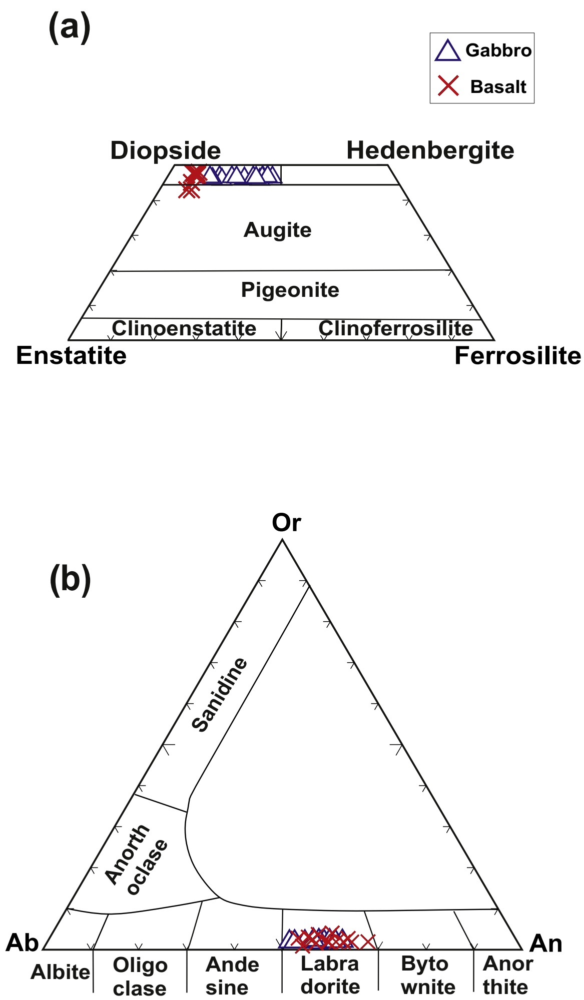

Fig. 5. (a) Clinopyroxene compositions (Morimoto, 1988) in the gabbroic and basaltic rocks. The crystals fall in the diopside to augite fields. (b) Plagioclase compositions (Deer et al., 1991) the crystals plot in the labradorite field.

and pillow (Fig. 3f,g). Some researchers, based on geochemical data, have suggested the mafic lava as MORB and OIB source in an intraplate tectonic setting and based on concomitance with ophiolite have interpreted that this complex is part of the Zagros ophiolite which obducted in the Late Cretaceous (Ghazi and Hassanipak, 1999; Allahyari et al., 2012; Saccani et al., 2013). These unites are mostly brecciated and mélange with unconsolidated sediments and peperite type rocks that contain some Nummulites and remnant fossils (Fig. 3h, i) of the Eocene age. In western Noorabad, some basaltic rocks are replaced with green schist and/or changed to red and oxidized in the fault zone. Far from the fault, the primary magmatic texture is preserved. Primary textures and structures such as lava flow and pillow for mafic rocks show that the eruption occurred in submarine basin.

In these areas some pillow lava and peperite are in direct contact with each other. They are deformed and primary limestone sediments are located between the pillows suggesting that some of the pillows formed within the sediments. The formation of pillow-like basalts in the area suggests that the sediments were completely unconsolidated and water-saturated.

3. Petrography

Based on our field observations, the Harsin-Noorabad mafic rocks are divided into two types and are described below.

3.1. Gabbro

The gabbros are mostly heterogeneous blocks near Noorabad. The gabbros are mostly fine- to coarse-grained and are affected by dynamic deformation. Granular and micro-granular textures are common (Fig. 4a,b). The weathered surfaces are generally gray to green and are fractured. The rocks are mainly composed of plagioclase and pyroxene, (Fig. 4c,d). The plagioclase grains are euhedral to subhedral and show polysynthetic twining (Fig. 4c,d) and are locally saussuritized. The pyroxenes generally exhibit clear cleavage traces and are subhedral shapes (Fig. 4d), and some parts are altered to actinolite and chlorite (Fig. 4e).

3.2. Basalt

The basalts are composed of a fine-grained groundmass of plagioclase and clinopyroxene with microlites and occasional plagioclase microphenocrysts (Fig. 4f,g). Most of the rocks show some amygdaloidal textures that are filled by calcite (Fig. 4f). The clinopyroxenes occur as quenched forms between plagioclase microlites. Most of the plagioclases are saussuritized and are partially replaced by epidote. The plagioclase microphenocrysts are generally assemblage minerals with irregular borders and are skeletal and acicular shapes (Fig. 4h).

In the peperites, most of the plagioclase and pyroxene grains are broken and crushed in the calcite groundmass (Fig. 4i). The fractures and cavities of the rocks are filled by calcite and chlorite.

4. Analytical techniques

The samples are chosen for the chemical analyses based on their location and apparent freshness. Because most of the basaltic rocks had amygdaloidal textures and contained veins, the secondary calcites in the basaltic rocks were first removed by 10% acetic acid (CH_3COOH), and the treated samples were then washed with ultrapure water. The major element contents of whole rocks were determined by the conventional X-ray fluorescence (XRF) technique with a Rigaku ZSX Primus II at Nagoya University (mixture of 0.5 gr sample powder and 5.0 gr lithium tetraborate). The mixture was melted at 1200 °C for 12–17 min with a high frequency bead sampler. The loss on ignition (LOI) of the sample was calculated by the weight difference after ignition at 950 °C. To determine the trace element abundances including rare earth elements (REEs) and Sr-Nd isotope ratios, 100–200 mg of the powdered sample was completely dissolved in 3 ml of HF (38%) and 0.5–1 ml of $HClO_4$ (70%) in a covered PTFE beaker at 120–140 °C on a hotplate in a clean room. The dissolved sample was then dried at 140 °C on the hotplate with infrared lamps. The dried sample was dissolved in 5–10 ml of 2.4 M HCl, and the resulting solution was used for analyses of the trace elements and isotopes.

The concentrations of the trace elements were analyzed by inductively coupled plasma mass spectrometry (ICP-MS) (Agilent 7700x) at Nagoya University. The isotope ratios of Sr and Nd were determined by VG Sector 54-30 and GVI IsoProbe-T thermal ionization mass spectrometers (TIMS) at Nagoya University. The mass fractionations during measurement were corrected according to $^{86}Sr/^{88}Sr = 0.1194$ and $^{146}Nd/^{144}Nd = 0.7219$. The NBS987 and JNdi-1 standards (Tanaka et al., 2000) were adapted as the natural Sr and Nd isotope ratio standards, respectively. Detailed descriptions of the analytical techniques are provided in Azizi and Asahara (2013) and Nouri et al. (2016).

The chemical compositions of fresh clinopyroxene and plagioclase grains were determined by a JXA-8800R electron microprobe analyzer (EPMA) at Nagoya University. The acceleration voltage and beam current were set at 15 kV and 12 nA, respectively.

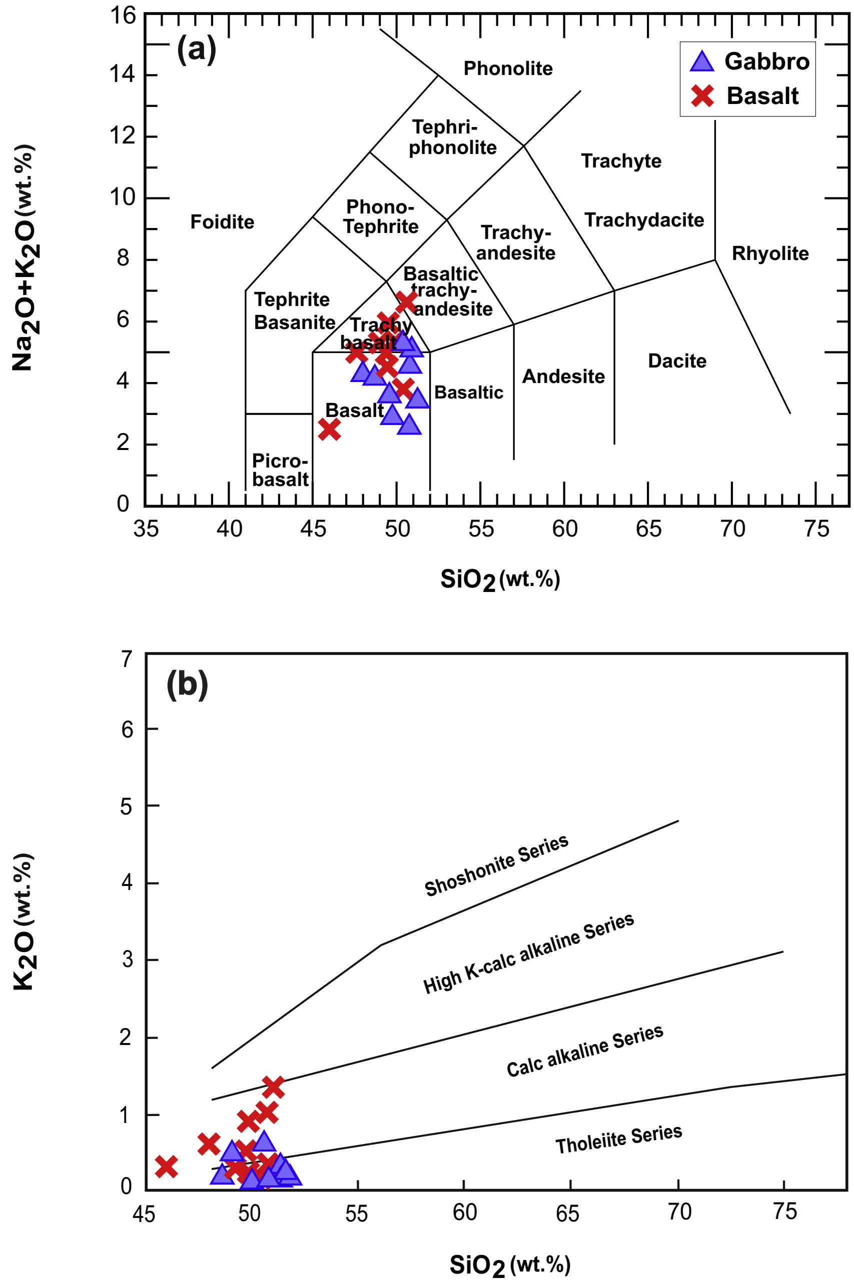

Fig. 6. (a) Classification of Le Bas et al. (1986), the samples plot in the basalt to trachybasalt fields (b) K_2O (wt.%) – SiO_2 (wt.%) diagram (Peccerillo and Taylor, 1976).

5. Mineral chemistry

The chemical compositions of the clinopyroxene and plagioclase in the Harsin-Noorabad mafic rocks are shown in Tables 1a and 1b.

5.1. Clinopyroxene

Most of the clinopyroxenes in the gabbros are unzoned (Table 1a). The clinopyroxenes are characterized by high contents of Al_2O_3 (1.2–10.8 wt.%) and Na_2O (0.1–1.7 wt.%), low Cr_2O_3 contents (<0.1 wt.%) and low Mg# (0.62–0.75). They plot in the diopside field on the wollastonite-enstatite-ferrosilite ternary diagram (Fig. 5a; Morimoto, 1988), and their compositions are Wo_{43-54}, En_{27-44}, and Fs_{13-27}.

Clinopyroxenes from the Harsin basalts are characterized by compositional variability such as Al_2O_3 contents (2.6–4.1 wt.%) and Na_2O contents (0.4–0.5 wt.%). Most of clinopyroxenes plot within the field of diopside to augite (fig. 5a) in the diagram of Morimoto (1988).

5.2. Plagioclase

The plagioclases are generally unzoned. Their CaO contents (10.4–14.1 wt.%) and Na_2O contents (3.6–5.7 wt.%) do not show large variations (Table 1b). The anorthite content ranges from 53 to 68 wt.%. In the Ab-Or-An ternary diagram (Deer et al., 1991), all of the minerals plot in the labradorite field (Fig. 5b).

The analyzed fresh plagioclase grains in the basalts are composed of $An_{53.8-65.8}$ $Ab_{30.9-45.0}$ and $Or_{0.30-1.17}$ with Al_2O_3 contents ranging between 30.4–31.0 wt.%. Most of the plagioclase compositions plot within the labradorite field on the Ab-Or-An ternary diagram (Fig. 5b; Deer et al., 1991).

Table 1a
Clinopyroxene composition by EPMA.

Location: Noorabad											
Rock type						Gabbro					
Sample name			IR-FNG21					IR-FNG35			
Grain	N1	N2	N3	N4	N5	N6	N7	N8	N9	N10	N11
Point	1	2	3	4	5	6	7	8	9	10	11
SiO_2 wt.%	49.38	50.72	50.78	50.43	47.09	50.37	49.35	51.89	54.68	56.37	49.94
TiO_2	0.408	0.407	0.425	0.277	0.261	1.189	0.428	0.381	0.324	0.091	0.501
Al_2O_3	8.299	5.630	5.575	5.313	10.798	6.127	7.948	4.508	3.252	1.188	6.882
Cr_2O_3	0.045	0.066	0.112	0.038	0.003	0.066	nd	0.128	0.059	0.023	0.040
FeO	12.09	14.94	13.73	14.22	12.77	12.13	13.02	13.71	12.66	10.42	13.47
MnO	0.208	0.242	0.233	0.258	0.168	0.280	0.247	0.267	0.262	0.151	0.307
MgO	14.66	13.98	14.38	14.03	12.91	15.11	12.18	14.52	15.35	17.63	14.18
CaO	12.08	11.59	11.90	11.86	11.99	12.00	13.04	11.98	12.14	12.70	11.64
Na_2O	1.350	0.845	1.029	0.815	1.772	1.061	0.952	0.779	0.463	0.148	1.053
K_2O	0.089	0.063	0.054	0.087	0.123	0.049	0.075	0.041	0.038	0.015	0.058
Total	98.61	98.51	98.28	97.36	97.91	98.38	97.25	98.20	99.28	98.81	98.08
Cation											
Si	1.845	1.915	1.915	1.924	1.784	1.886	1.879	1.953	2.015	2.064	1.884
Ti	0.011	0.012	0.012	0.008	0.007	0.033	0.012	0.011	0.009	0.003	0.014
Al (total)	0.366	0.251	0.248	0.239	0.482	0.270	0.357	0.200	0.141	0.051	0.306
Mn	0.007	0.008	0.007	0.008	0.005	0.009	0.008	0.009	0.008	0.005	0.010
Mg	0.817	0.787	0.808	0.798	0.729	0.843	0.691	0.815	0.843	0.962	0.798
Ca	0.484	0.469	0.481	0.485	0.487	0.481	0.532	0.483	0.479	0.498	0.471
Na	0.098	0.062	0.075	0.060	0.130	0.077	0.070	0.057	0.033	0.011	0.077
K	0.004	0.003	0.003	0.004	0.006	0.002	0.004	0.002	0.002	0.001	0.003
Cr	0.001	0.002	0.003	0.001	0.000	0.002	0.000	0.004	0.002	0.001	0.001
Fe^{3+}	0.017	0.000	0.000	0.000	0.065	0.000	0.000	0.000	0.000	0.000	0.000
Fe^{2+}	0.361	0.472	0.433	0.454	0.340	0.380	0.415	0.431	0.390	0.319	0.425
Total	4.011	3.980	3.986	3.981	4.035	3.984	3.967	3.964	3.922	3.914	3.988
Al(IV)	0.155	0.085	0.085	0.076	0.216	0.114	0.121	0.047	−0.015	−0.064	0.116
Al(VI)	0.211	0.166	0.163	0.162	0.266	0.156	0.236	0.153	0.156	0.115	0.190
$Mg^{\#}$	0.68	0.62	0.65	0.63	0.64	0.68	0.62	0.65	0.68	0.75	0.65
End member											
Wo	48.7	45.6	46.9	46.0	45.0	49.5	42.7	47.1	49.2	54.1	47.1
En	28.8	27.1	27.9	27.9	30.0	28.2	43.9	27.9	28.0	28.0	27.8
Fs	22.5	27.3	25.1	26.1	25.0	22.3	13.4	24.9	22.8	17.9	25.1

Location: Harsin											
Rock type	Basalt										
Sample name	FNG8					FNG12					
Grain	H1	H2	H3	H4	H5	H6	H7	H8	H9	H10	H11
Point	1	2	3	4	5	6	7	8	9	10	11
SiO_2 wt.%	52.50	52.08	51.34	52.30	52.93	52.59	53.20	51.43	51.77	52.57	52.83
TiO_2	0.448	0.514	0.663	0.993	0.732	0.823	0.664	0.919	0.642	0.767	0.576
Al_2O_3	3.200	3.173	3.813	3.032	2.594	3.013	2.555	3.157	4.090	3.044	3.054
Cr_2O_3	0.724	0.877	0.56	0.098	0.506	0.549	0.425	0.537	0.807	0.388	0.354
FeO	4.757	4.736	5.182	5.289	5.282	5.426	5.194	5.074	5.163	5.174	5.679
MnO	0.137	0.106	0.103	0.198	0.125	0.194	0.194	0.195	0.14	0.152	0.191
MgO	15.80	15.39	16.37	15.88	16.09	15.77	15.60	15.36	16.92	15.83	16.67
CaO	21.71	22.01	20.97	22.14	21.95	21.79	22.48	22.02	20.18	22.00	20.22
Na_2O	0.441	0.537	0.520	0.440	0.495	0.535	0.493	0.501	0.464	0.501	0.457
K_2O	0.004	0.013	nd	nd	0.005	0.004	0.014	0.015	nd	0.003	0.001
Total	99.72	99.44	99.52	100.39	100.71	100.74	100.83	99.27	100.22	100.44	100.09
Cation											
Si	1.926	1.921	1.891	1.914	1.929	1.918	1.938	1.906	1.889	1.921	1.930
Ti	0.012	0.014	0.018	0.027	0.020	0.023	0.018	0.026	0.018	0.021	0.016
Al (total)	0.138	0.138	0.166	0.131	0.111	0.130	0.110	0.138	0.176	0.131	0.132
Mn	0.004	0.003	0.003	0.006	0.004	0.006	0.006	0.006	0.004	0.005	0.006
Mg	0.864	0.846	0.899	0.866	0.874	0.858	0.847	0.849	0.920	0.862	0.908
Ca	0.854	0.870	0.828	0.868	0.857	0.852	0.877	0.874	0.789	0.861	0.791
Na	0.031	0.038	0.037	0.031	0.035	0.038	0.035	0.036	0.033	0.035	0.032
K	0.000	0.001	0.000	0.000	0.000	0.000	0.001	0.001	0.000	0.000	0.000
Cr	0.021	0.026	0.016	0.003	0.015	0.016	0.012	0.016	0.023	0.011	0.010
Fe^{3+}	0.000	0.005	0.036	0.016	0.011	0.010	0.001	0.018	0.020	0.010	0.000
Fe^{2+}	0.146	0.146	0.105	0.138	0.144	0.150	0.156	0.130	0.127	0.143	0.174
Total	3.998	4.008	3.999	4.000	4.000	4.000	4.000	4.000	3.999	4.000	4.000
Al(IV)	0.074	0.079	0.109	0.086	0.071	0.082	0.062	0.094	0.111	0.079	0.070
Al(VI)	0.065	0.059	0.057	0.044	0.040	0.048	0.047	0.044	0.065	0.052	0.062
Mg#	0.86	0.85	0.85	0.84	0.84	0.84	0.84	0.84	0.85	0.84	0.84
End member											
Wo	45.8	45.8	43.9	45.8	45.3	45.4	46.6	46.5	42.3	45.8	42.3
En	46.4	46.4	47.7	45.7	46.2	45.7	45.0	45.1	49.3	45.8	48.5
Fs	7.83	7.83	8.46	8.54	8.51	8.83	8.41	8.36	8.44	8.40	9.27

nd = not detected.
Wo = Wollastonite; En = Enstatite; Fs = Ferrosilite.
Structural formula based on 6 oxygen atoms.

Table 1b
Plagioclase composition by EPMA.

Location: Noorabad											
Rock type	Gabbro										
Sample name	IR-FNG21					IR-FNG35					
Grain	P1	P2	P3	P4	P5	P6	P7	P8	P9	P10	P11
Point	1	2	3	4	5	6	7	8	9	10	11
SiO_2 wt.%	55.74	56.43	55.05	54.84	55.72	54.99	51.83	55.73	56.43	55.70	55.63
TiO_2	0.062	0.090	0.095	0.052	0.071	0.048	0.009	0.100	0.058	0.073	0.049
Al_2O_3	28.99	28.26	29.25	28.96	29.70	29.75	31.16	28.80	28.62	29.02	29.66
FeO	0.416	0.235	0.476	0.523	0.278	0.191	0.425	0.451	0.309	0.278	0.139
MnO	0.009	nd	nd	nd	nd	0.010	0.021	0.037	nd	nd	nd
MgO	0.019	0.021	0.031	0.047	0.075	0.013	0.002	0.037	0.031	0.007	nd
CaO	11.23	10.42	11.71	11.65	11.17	11.72	14.10	11.04	10.67	11.21	11.55
Na_2O	5.457	5.693	5.019	4.901	4.887	5.063	3.612	5.348	5.598	5.247	5.237
K_2O	0.045	0.027	0.025	0.071	0.100	0.010	0.030	0.019	0.045	0.024	0.010
Total	101.99	101.19	101.70	101.05	102.06	101.81	101.20	101.62	101.78	101.56	102.27
Cation											
Si	2.466	2.513	2.449	2.457	2.472	2.440	2.333	2.478	2.500	2.478	2.456
Ti	0.002	0.003	0.003	0.002	0.002	0.002	0.000	0.003	0.002	0.002	0.002
Al	1.512	1.483	1.534	1.529	1.553	1.556	1.653	1.509	1.495	1.521	1.543
Fe^{3+}	0.000	0.000	0.000	0.000	0.000	0.000	0.000	0.000	0.000	0.000	0.000
Fe^{2+}	0.015	0.009	0.018	0.020	0.010	0.007	0.016	0.017	0.011	0.010	0.005
Mg	0.001	0.001	0.002	0.003	0.005	0.001	0.000	0.002	0.002	0.000	0.000
Ca	0.532	0.497	0.558	0.559	0.531	0.557	0.680	0.526	0.506	0.534	0.546
Na	0.468	0.492	0.433	0.426	0.420	0.436	0.315	0.461	0.481	0.452	0.448
K	0.003	0.002	0.001	0.004	0.006	0.001	0.002	0.001	0.003	0.001	0.001
Total	5.000	4.999	4.999	5.000	4.999	4.999	4.999	4.999	5.000	5.000	5.000
End member											
An	53.1	50.2	56.2	56.5	55.5	56.1	68.2	53.2	51.2	54.1	54.9
Ab	46.7	49.6	43.6	43.0	43.9	43.9	31.6	46.7	48.6	45.8	45.1
Or	0.253	0.155	0.143	0.410	0.591	0.057	0.173	0.109	0.257	0.138	0.057

Location: Harsin														
Rock type	Basalt													
Sample name	FNG8							FNG12						
Grain	P1	P2	P3	P4	P5	P6	P7	P8	P9	P10	P11	P12	P13	P14
Point	1	2	3	4	5	6	7	8	9	10	11	12	13	14
SiO_2 wt.%	54.54	53.40	52.13	53.16	53.93	52.64	54.70	51.13	52.05	52.60	52.20	52.45	51.97	53.26
TiO_2	0.035	0.031	0.069	0.034	0.080	0.090	0.066	0.026	0.047	0.086	0.080	0.090	0.069	0.015
Al_2O_3	30.43	30.57	30.74	30.37	30.11	29.78	31.41	31.06	30.49	30.81	30.46	30.81	30.98	30.61
FeO	0.196	0.172	0.171	0.191	0.123	0.197	0.210	0.143	0.156	0.177	0.176	0.209	0.186	0.148
MnO	nd	nd	0.020	0.006	0.022	nd	nd	nd	0.008	0.034	0.045	nd	0.011	nd
MgO	0.015	0.007	0.023	0.018	0.039	0.019	0.050	0.044	0.019	0.025	nd	0.021	0.012	0.015
CaO	12.64	12.86	13.12	12.60	12.54	12.35	9.91	14.21	12.77	13.12	13.04	13.43	13.58	12.82
Na_2O	4.545	4.294	4.096	4.492	4.595	4.484	4.578	3.527	4.334	4.084	4.369	3.890	3.869	4.418
K_2O	0.061	0.057	0.046	0.052	0.068	0.060	0.182	0.057	0.052	0.079	0.052	0.046	0.059	0.058
Total	102.52	101.39	100.41	100.98	101.57	99.62	101.13	100.24	99.94	101.06	100.41	100.95	100.76	101.36
Cation														
Si	2.412	2.388	2.355	2.385	2.405	2.393	2.447	2.322	2.359	2.363	2.355	2.362	2.344	2.380
Ti	0.001	0.001	0.002	0.001	0.003	0.003	0.002	0.001	0.002	0.003	0.003	0.003	0.002	0.001
Al	1.586	1.611	1.637	1.606	1.583	1.595	1.656	1.662	1.628	1.631	1.619	1.635	1.647	1.612
Ca	0.599	0.616	0.635	0.606	0.599	0.601	0.475	0.691	0.620	0.631	0.630	0.648	0.656	0.614
Na	0.390	0.372	0.359	0.391	0.397	0.395	0.397	0.311	0.381	0.356	0.382	0.340	0.338	0.383
K	0.003	0.003	0.003	0.003	0.004	0.003	0.010	0.003	0.003	0.005	0.003	0.003	0.003	0.003
Total	4.991	4.993	4.991	4.991	4.991	4.991	4.989	4.990	4.992	4.989	4.992	4.991	4.992	4.993
End member														
An	60.4	62.1	63.7	60.6	59.9	60.1	53.8	68.8	61.8	63.7	62.1	65.4	65.8	61.4
Ab	39.3	37.5	36.0	39.1	39.7	39.5	45.0	30.9	37.9	35.9	37.6	34.3	33.9	38.3
Or	0.347	0.328	0.266	0.298	0.387	0.348	1.177	0.328	0.300	0.457	0.295	0.267	0.340	0.331

nd = not detected.
Ab = Albite; An = Anorthite; Or = Orthoclase.
Structural formula based on 8 oxygen atoms.

6. Geochemical characteristics

The results of the chemical composition of 18 whole rock samples are listed in Table 2. The gabbro samples contain 46.1–51.0 wt.% SiO_2, 12.8–18.8 wt.% Al_2O_3, 0.4–2.7 wt.% TiO_2 and 3.9–10.1 wt.% MgO, and the basalt samples 47.9–50.8 wt.% SiO_2, 12.3–16.2 wt.% Al_2O_3, 1.6–3.0 wt.% TiO_2 and 3.7–5.9 wt.% MgO. Some gabbro and basalt samples have high Nb content (Ave(Nb) = 15.1 ppm) with higher contents of TiO_2 (1.1–3.0 wt.%), suggesting a similarity to Nb-enriched arc basalts (Wang et al., 2011, 2013; Zhang et al., 2012).

Table 2
Chemical composition of whole rocks.

Sample	HV1	HV3	HV4	GN1	GN2	FNG3	FNG4	FNG5	FNG7
Rock type	Basalt	Gabbro	Basalt	Gabbro	Gabbro	Basalt	Basalt	Gabbro	Gabbro
Location	Noorabad	Noorabad	Noorabad	Noorabad	Noorabad	Noorabad	Noorabad	Noorabad	Noorabad
SiO_2 (wt.%)	49.10	48.47	49.98	50.89	50.28	46.09	50.79	49.04	50.83
TiO_2	2.68	0.42	1.14	0.54	1.58	0.99	1.63	1.27	1.10
Al_2O_3	12.78	16.49	16.79	16.22	15.84	16.96	16.23	16.16	16.62
Fe_2O_3	14.90	5.26	8.00	5.25	9.45	10.61	9.86	8.68	7.42
MnO	0.11	0.10	0.17	0.11	0.17	0.17	0.12	0.15	0.14
MgO	3.89	9.08	8.30	8.61	6.65	7.25	4.79	6.29	6.78
CaO	4.83	14.57	10.13	14.46	9.67	12.12	6.66	11.55	10.23
Na_2O	5.06	3.81	3.60	2.52	3.69	2.22	5.02	3.59	4.06
K_2O	0.31	0.18	0.11	0.10	0.67	0.33	1.55	0.45	0.31
P_2O_5	0.59	0.033	0.13	0.031	0.22	0.10	0.34	0.26	0.17
LOI	5.96	1.61	1.63	1.27	1.80	2.93	2.06	0.90	1.68
Total	100.22	100.01	99.98	99.99	100.02	99.77	99.07	98.34	99.34
V (ppm)	253	128	172	181	208	358	226	156	140
Cr	23.8	551	154	402	167	58.3	9.76	83.4	172
Co	24.1	28.4	33.3	26.7	32.8	43.6	26.2	29.4	32.9
Ni	14.1	197	143	135	101	55.0	9.90	61.7	114
Cu	28.0	81.4	9.05	158	42.0	5.38	18.2	13.0	93.8
Zn	91.6	35.9	60.5	37.1	86.4	62.5	80.7	69.1	89.7
Ga	25.6	12.7	13.6	12.0	17.0	15.3	17.0	16.1	17.6
Rb	3.67	1.66	1.50	1.75	19.4	11.3	44.5	8.02	7.14
Sr	183	241	225	170	184	1630	339	291	264
Zr	189	19.3	71.2	23.0	58.6	65.9	161	119	150
Nb	39.0	2.64	7.76	2.42	11.6	3.52	7.92	5.16	7.82
Cs	0.107	0.048	0.041	0.130	0.387	0.912	0.641	0.211	0.119
Ba	37.9	24.4	37.4	27.3	115	118	345	88.1	94.4
Pb	0.983	1.00	1.34	0.82	1.94	2.56	3.28	3.46	4.10
Th	3.33	0.210	0.542	0.294	2.03	1.52	4.98	2.76	3.07
U	0.629	0.039	0.094	0.071	0.499	0.346	1.37	0.722	0.991
Hf	*	*	*	*	*	1.99	4.16	4.03	3.63
Ta	2.24	0.175	0.515	0.285	0.630	0.236	0.560	0.354	0.514
Y	46.9	8.52	19.7	13.5	31.6	23.3	25.6	26.7	29.6
La (ppm)	31.3	1.19	5.20	1.84	10.4	6.06	16.8	12.3	12.2
Ce	70.0	3.19	13.4	4.89	24.4	14.0	33.9	26.7	27.6
Pr	8.62	0.512	1.93	0.767	3.33	1.88	4.15	3.47	3.67
Nd	35.2	2.58	9.04	4.04	15.6	8.84	17.2	15.1	16.4
Sm	6.50	0.650	2.05	1.22	4.20	2.55	3.77	3.67	3.90
Eu	2.03	0.350	0.78	0.554	1.42	0.895	1.35	1.22	1.30
Gd	8.05	1.04	2.71	1.77	5.05	3.57	4.42	4.53	4.89
Tb	1.45	0.222	0.531	0.356	0.88	0.608	0.718	0.75	0.81
Dy	9.46	1.58	3.66	2.56	5.93	4.20	4.70	4.91	5.40
Ho	1.89	0.337	0.754	0.548	1.24	0.915	0.982	1.03	1.13
Er	5.21	0.951	2.24	1.58	3.52	2.73	2.87	2.99	3.35
Tm	0.722	0.135	0.300	0.217	0.486	0.396	0.412	0.428	0.477
Yb	4.45	0.848	1.98	1.38	3.06	2.80	2.73	2.76	3.11
Lu	0.634	0.120	0.282	0.190	0.417	0.400	0.402	0.401	0.456
Mg#	34.1	77.4	67.3	76.5	58.2	57.5	45.9	58.9	60.7
Ba/Th	11.4	116	69.1	92.8	56.7	77.4	69.2	31.9	30.7
Th/Nb	0.085	0.080	0.070	0.122	0.176	0.433	0.629	0.536	0.393
Th/Nd	0.094	0.082	0.060	0.073	0.131	0.172	0.290	0.183	0.188
Nb/U	62.0	67.8	82.8	34.1	23.2	10.2	5.8	7.1	7.9

Sample	FNG10	FNG29	FNG31	FNG51	FNG52	FNG63	FNG64	FNG65	FNG66
Rock type	Gabbro	Gabbro	Gabbro	Basalt	Basalt	Basalt	Basalt	Basalt	Basalt
Location	Noorabad	Noorabad	Noorabad	Harsin	Harsin	Harsin	Harsin	Harsin	Harsin
SiO_2 (wt.%)	49.76	49.73	51.02	50.41	50.37	49.58	47.90	49.66	49.41
TiO_2	0.48	1.03	0.58	2.07	2.30	2.95	2.82	1.75	1.75
Al_2O_3	15.30	16.06	18.78	13.41	14.27	12.54	12.28	13.46	13.44
Fe_2O_3	5.88	6.92	6.10	11.92	10.81	14.57	16.46	12.72	13.38
MnO	0.10	0.09	0.11	0.27	0.25	0.25	0.21	0.22	0.22
MgO	10.12	10.04	7.29	4.66	5.88	3.73	4.50	5.35	5.69
CaO	14.04	9.46	11.96	8.07	9.39	6.80	5.97	7.73	7.49
Na_2O	2.71	3.52	3.24	4.88	3.77	4.66	4.35	4.59	4.34
K_2O	0.093	0.10	0.063	0.37	1.10	1.02	0.65	0.16	0.51
P_2O_5	0.035	0.14	0.050	0.28	0.35	0.42	0.40	0.20	0.20
LOI	1.40	2.07	1.32	2.85	1.18	2.66	3.78	3.86	2.73
Total	99.91	99.15	100.52	99.19	99.67	99.17	99.31	99.70	99.17
V (ppm)	121	170	155	331	368	410	420	315	322
Cr	578	363	128	36.9	38.5	51.0	56.7	118	115
Co	36.3	40.9	31.9	41.1	44.1	45.1	46.0	40.6	41.9
Ni	288	277	103	45.3	47.6	33.9	35.6	39.3	40.0

Table 2 (*Continued*)

Sample Rock type Location	FNG10 Gabbro Noorabad	FNG29 Gabbro Noorabad	FNG31 Gabbro Noorabad	FNG51 Basalt Harsin	FNG52 Basalt Harsin	FNG63 Basalt Harsin	FNG64 Basalt Harsin	FNG65 Basalt Harsin	FNG66 Basalt Harsin
Cu	64.9	10.7	92.1	126	138	86.4	78.9	88.9	91.2
Zn	49.6	38.5	53.2	112	125	160	161	109	112
Ga	11.8	11.3	15.1	17.5	20.7	20.0	22.1	18.9	17.3
Rb	2.49	1.60	1.42	3.27	25.5	16.2	12.5	3.84	9.64
Sr	281	312	193	295	272	253	232	196	548
Zr	21.8	89.4	27.1	152	178	251	272	164	166
Nb	0.35	1.51	0.61	16.7	19.8	21.3	22.7	6.79	5.09
Cs	0.084	0.037	0.032	0.019	0.180	0.031	0.028	0.027	0.042
Ba	25.5	25.6	19.7	55.8	177	110	232	50.4	301
Pb	1.77	0.432	0.825	1.90	2.68	1.86	2.83	1.66	2.81
Th	0.195	0.152	0.120	2.11	3.09	3.45	3.58	1.54	1.56
U	0.058	0.059	0.035	0.465	0.957	0.847	0.807	0.355	0.363
Hf	0.907	2.23	0.909	4.18	4.99	7.01	6.78	4.66	4.71
Ta	0.029	0.118	0.051	1.04	1.35	1.43	1.14	0.329	0.331
Y	13.4	20.1	13.1	34.7	37.9	53.0	33.2	42.6	42.3
La (ppm)	1.82	3.85	1.28	16.9	19.1	19.5	13.5	10.2	10.0
Ce	5.07	11.7	4.18	36.2	41.3	46.3	29.5	25.0	24.8
Pr	0.84	1.81	0.728	4.75	5.36	6.18	3.91	3.57	3.51
Nd	4.63	9.10	4.10	21.1	23.6	28.1	17.8	17.1	16.9
Sm	1.53	2.52	1.35	4.88	5.32	7.05	4.56	4.58	4.46
Eu	0.71	1.06	0.719	1.70	1.87	2.31	1.45	1.55	1.49
Gd	2.26	3.42	2.09	6.08	6.68	9.08	5.76	6.48	6.38
Tb	0.38	0.564	0.360	1.01	1.11	1.48	0.937	1.13	1.13
Dy	2.54	3.75	2.44	6.57	7.32	9.72	6.16	7.78	7.73
Ho	0.535	0.782	0.52	1.36	1.51	2.05	1.31	1.68	1.66
Er	1.51	2.27	1.48	3.90	4.28	6.01	3.81	4.97	4.92
Tm	0.209	0.314	0.205	0.553	0.599	0.849	0.548	0.717	0.719
Yb	1.34	2.04	1.33	3.80	4.66	4.70	3.59	4.66	4.69
Lu	0.193	0.293	0.192	0.547	0.690	0.690	0.532	0.688	0.686
Mg#	77.3	74.2	70.3	43.6	41.5	33.6	35.1	45.4	45.7
Ba/Th	131	168	164	26.5	57.3	31.7	64.7	32.6	194
Th/Nb	0.555	0.101	0.197	0.126	0.156	0.162	0.158	0.227	0.306
Th/Nd	0.042	0.017	0.029	0.100	0.131	0.123	0.201	0.090	0.092
Nb/U	6.0	25.6	17.4	35.9	20.7	25.1	28.1	19.1	14.0

Mg# = 100Mg/(Mg + Fe).
[*] Not measured.

According to the classification of LeBas et al. (1986), the samples plot in the basalt to trachybasalt fields (Fig. 6a). In this diagram, the samples are mainly in the field of basalt, and two samples are in the alkali basalt field. In the SiO_2 versus K_2O diagram (Peccerillo and Taylor, 1976), the samples plot in the tholeiitic and clac-alkaline fields (Fig. 6b).

On the NMORB normalized spider diagram (Sun and McDonough, 1989), the samples are characterized by negative anomalies of Nb and positive anomalies of large-ion lithophile elements (LILEs) such as Sr, K and Ba (Fig. 7a). Some samples show weak depletions in Nb, and others show large depletions in Nb. In the Chondrite normalized diagram, some samples exhibit flat REE patterns (Fig. 7b) and are similar to the Mariana Trough back arc basin basalts (BABBs) and NMORB. In this diagram, some samples exhibit steeper light rare earth element/heavy rare earth element (LREE/HREE) patterns than other samples and are a similar trend (Fig. 7b) to the Okinawa trough BABBs (Shinjo et al., 1999), EMORB and Nb-enriched arc basalts (NEBs) from Yunkai (Zhang et al., 2012; Wang et al., 2013).

7. Sr-Nd isotope ratios

The Sr-Nd isotope ratios of 18 samples in the study area are listed in Table 3. Because Braud (1978) and Shahidi and Nazari (1997) reported that the fragmented mafic lava flows, pillows and pyroclastics were interbedded with red to green sandy limestone and shale with some Eocene fossils, the initial isotope ratios were calculated based on an age of 45 Ma. For the gabbro samples, the $^{87}Sr/^{86}Sr(i)$ ratios and $\varepsilon Nd(t)$ values are 0.7032–0.7071 and +3.8 to +9.9, respectively and for basalt samples these values are 0.7039–0.7057 and +4.4 to +8.5, respectively. The gabbros and basalts have similar isotope characteristics. The $^{87}Sr/^{86}Sr(i)$–$\varepsilon Nd(t)$ and $^{87}Sr/^{86}Sr(i)$-$^{143}Nd/^{144}Nd(i)$ diagrams (Fig. 8a,b) shows that the samples plot near the depleted mantle and that the samples were affected by enriched mantle 2 (EMII) components. In this diagram (Fig. 8a), the Harsin-Noorabad samples mostly overlap with the Kamyaran mafic rocks domain, Neyriz, Mawat and Baft ophiolites (Azizi et al., 2011b, 2013; Shafaii Moghadam et al., 2013, 2014) but show a different trend from the other domains. The EMII mantle component was considered to be a mantle contaminated by subducted continental and upper continental crust (Weaver, 1991; Greenough et al., 2005). These diagrams shows that the gabbros and basalts were not hardly affected by seawater alteration (Fig. 8a,b). The Nd model ages (T_{DM}) were calculated from the depleted mantle (Jahn et al., 1999) and vary from 159 to 766 Ma except for two samples (Table 3). The T_{DM} ages for all samples were similar.

The variations of $^{87}Sr/^{86}Sr(i)$ and $^{143}Nd/^{144}Nd(i)$ versus MgO (Fig. 8c,d) exhibit horizontal trends for the basalts and positive/negative correlations for the gabbros, respectively. The two diagrams indicate magmatic differentiation for the basalts and the contamination of the depleted mantle with a small continental fragment or slab component for the gabbros. The contamination was confirmed by the higher $^{87}Sr/^{86}Sr(i)$ and lower $\varepsilon Nd(t)$ values of some samples.

Table 3
Sr and Nd isotope ratios of whole rock samples.

Sample	Location	Group	Rb	Sr	^{87}Rb/^{86}Sr	^{87}Sr/^{86}Sr (p)	± 1SE	^{87}Sr/^{86}Sr (i)	Nd	Sm	^{147}Sm/^{144}Nd	^{143}Nd/^{144}Nd (p)	± 1SE	^{143}Nd/^{144}Nd (i)	εNd(0)	ε^{t}Nd	T_{DM} (Ma)
HV1	Noorabad	Basalt	3.67	183	0.0199	0.704547	0.000007	0.70453	6.50	35.2	0.152	0.513011	0.000024	0.51297	7.3	8.5	347
HV3	Noorabad	Gabbro	1.66	241	0.0193	0.703190	0.000007	0.70318	0.650	2.58	0.137	0.513070	0.000004	0.51303	8.4	9.7	159
HV4	Noorabad	Basalt	1.50	225	0.0298	0.703952	0.000008	0.70393	2.05	9.04	0.182	0.513002	0.000004	0.51295	7.1	8.3	715
GN1	Noorabad	Gabbro	1.75	170	0.306	0.704335	0.000007	0.70414	1.22	4.04	0.163	0.512931	0.000004	0.51288	5.7	6.9	659
GN2	Noorabad	Gabbro	19.4	184	0.3798	0.704743	0.000006	0.70450	4.20	15.6	0.133	0.512868	0.000004	0.51283	4.5	5.7	531
FNG3	Noorabad	Basalt	11.3	1628	0.0321	0.705430	0.000006	0.70541	2.55	8.84	0.140	0.512843	0.000005	0.51280	4.0	5.2	633
FNG4	Noorabad	Basalt	44.5	339	0.0798	0.704214	0.000008	0.70416	3.77	17.2	0.146	0.512915	0.000005	0.51287	5.4	6.6	533
FNG5	Noorabad	Gabbro	8.02	291	0.0784	0.704733	0.000008	0.70468	3.67	15.1	0.144	0.512935	0.000004	0.51289	5.8	7.0	471
FNG7	Noorabad	Gabbro	7.14	264	0.0257	0.704679	0.000007	0.70466	3.90	16.4	0.200	0.512990	0.000005	0.51293	6.9	8.1	1778
FNG10	Noorabad	Gabbro	2.49	281	0.0148	0.703973	0.000006	0.70396	1.53	4.63	0.167	0.513075	0.000004	0.51303	8.5	9.8	247
FNG29	Noorabad	Gabbro	1.60	312	0.0213	0.703547	0.000006	0.70353	2.52	9.10	0.199	0.513081	0.000005	0.51302	8.6	9.9	718
FNG31	Noorabad	Gabbro	1.42	193	0.0201	0.707115	0.000006	0.70710	1.35	4.10	0.175	0.512769	0.000004	0.51272	2.6	3.8	1480
FNG51	Harsin	Basalt	3.27	295	0.271	0.705544	0.000007	0.70537	4.88	21.1	0.136	0.512839	0.000004	0.51280	3.9	5.2	612
FNG52	Harsin	Basalt	25.5	272	0.185	0.705385	0.000007	0.70527	5.32	23.6	0.152	0.512841	0.000004	0.51280	4.0	5.2	761
FNG63	Harsin	Basalt	16.2	253	0.156	0.705274	0.000006	0.70517	7.05	28.1	0.155	0.512854	0.000004	0.51281	4.2	5.4	766
FNG64	Harsin	Basalt	12.5	232	0.0566	0.705455	0.000006	0.70542	4.56	17.8	0.162	0.512950	0.000005	0.51290	6.1	7.3	592
FNG65	Harsin	Basalt	3.84	196	0.0509	0.705453	0.000006	0.70542	4.58	17.1	0.160	0.512959	0.000004	0.51291	6.3	7.5	539
FNG66	Harsin	Basalt	9.64	548	0.0407	0.705721	0.000006	0.70570	4.46	16.9	0.156	0.512801	0.000005	0.51275	3.2	4.4	925

The Nd and Sr natural isotope ratios were normalized based on the ^{146}Nd/^{144}Nd = 0.7219 and ^{86}Sr/^{88}Sr = 0.1194. Average and 1σ for isotope ratio standards, JNdi-1 and NBS987 are ^{143}Nd/^{144}Nd = 0.512098 ± 0.00010 (n = 13) and ^{87}Sr/^{86}Sr = 0.710240 ± 0.000010 (n = 17). The CHUR (Chondritic Uniform Reservior) values, ^{147}Sm/^{144}Nd = 0.1967 and ^{143}Nd/^{144}Nd = 0.512638 were used to calculate the ε^0(DePaolo and Wasserburg, 1976).
The BABI (Basaltic Achondritic Best Initial = Bulk earth, undifferentiated) value, $T_{DM} = 1/\lambda$ Ln {[(^{143}Nd/^{144}Nd)sample-(^{143}Nd/^{144}Nd)$_{DM}$]/[(^{147}Sm/^{144}Nd)$_{sample}$-(^{147}Sm/^{144}Nd)$_{DM}$] + 1}. (^{143}Nd/^{144}Nd)$_{DM}$ = 0.51315, (^{147}Sm/^{144}Nd)$_{DM}$ = 0.2137. ε^0Nd = [((^{143}Nd/^{144}Nd)$_{sample}$/(^{143}Nd/^{144}Nd)$_{CHUR}$-1]*10000. (^{143}Nd/^{144}Nd)$_{CHUR}$ = 0.512638. ε^tNd = [((^{143}Nd/^{144}Nd)$_{sample(t)}$/(^{143}Nd/^{144}Nd)$_{CHUR(t)}$)-1]*10000, i = initial and p = present.

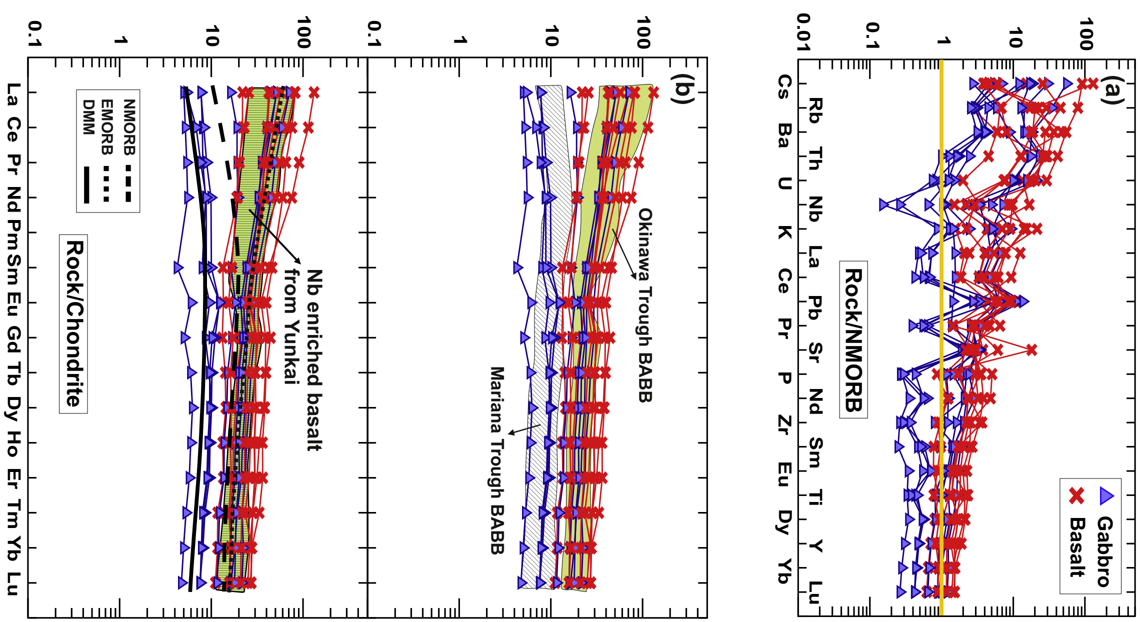

Fig. 7. (a) Normalized to NMORB value, respectively (Sun and McDonough, 1989). The most of the gabbro and some basalt samples are characterized by negative Nb anomalies and enrichment anomalies in LILE such as Sr, K and Ba. Most of the basalt samples and some gabbro samples show pronounced enrichments in the LILE such as Sr, K and Ba and weak depletions in Nb and Ta. (b) Chondrite normalized REE pattern. Chemical compositions of EMORB, NMORB and OIB are from Sun and McDonough (1989). Most of the gabbro samples have similar REE concentrations to NMORB, and most of the basalt samples have REE concentrations similar to EMORB and Nb-enriched basalt. Data sources are: for the Okinawa Trough BABB (back arc basin basalt) from Shinjo et al. (1999), Mariana Trough BABB from Pearce et al. (2005) and NEBs (Nb enriched basalts) from Yunkai are from Zhang et al. (2012).

8. Discussion

Mafic rocks are main key for distinguishing the different tectonic settings of magmatic rocks during the evolution of the Earth's crust. Based on the variation of major and trace elements, basaltic rocks have been divided in the different groups and many different diagrams are proposed by many researchers (Miyashiro, 1973; Ave Lallemant, 1976; Pearce et al., 1977; Coleman and Donato, 1979; Menzies et al., 1980; Gerlach et al., 1981; Verma et al., 2006; Pearce, 2008; Reagan et al., 2010; Whattam and Stern, 2011; Wang et al., 2013; Shen et al., 2014).

In the Ti versus V diagram (Fig. 9a; Shervais, 1982), most of the Harsin-Noorabad samples have high Ti/V ratios (20–50) that are similar to MORB and BABB (Reagan et al., 2010), although some

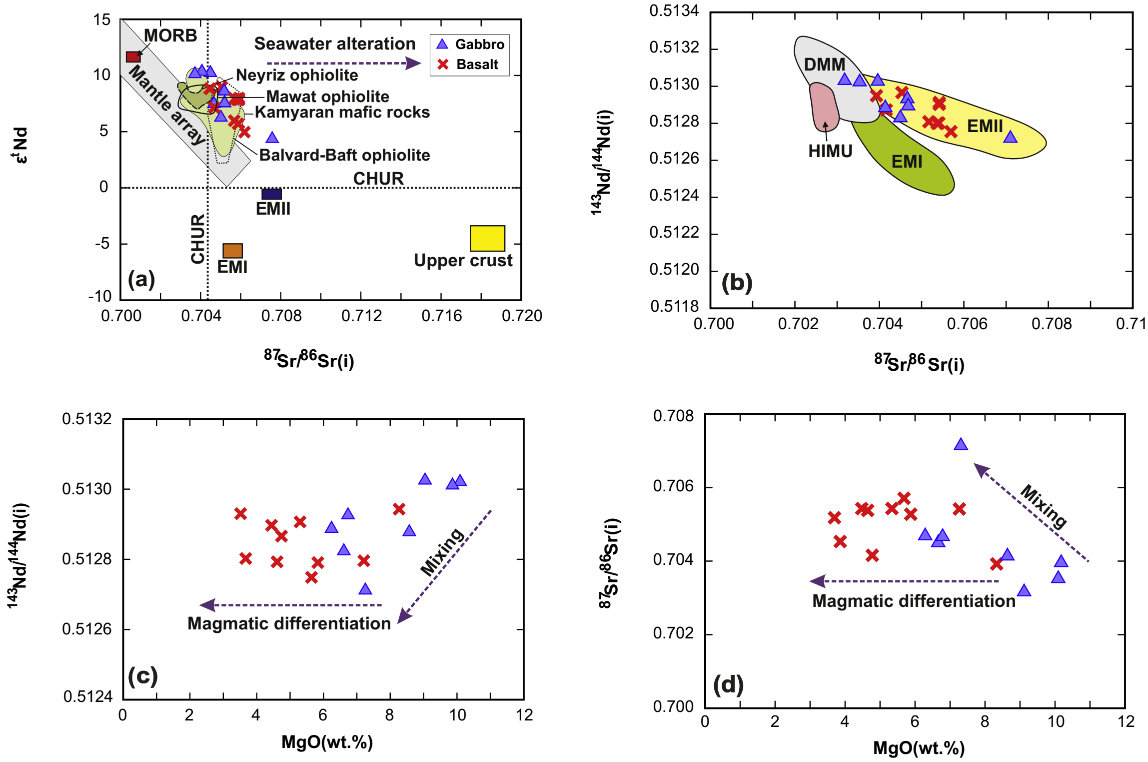

Fig. 8. (a) The variation of $^{87}Sr/^{86}Sr(i)$ versus $\varepsilon Nd(t)$. (b) The variation of $^{87}Sr/^{86}Sr(i)$-$^{143}Nd/^{144}Nd(i)$. Fields for mantle components are based on data compiled by Stracke et al. (2003) for Atlantic MORB (DMM), Saint Helena (HIMU), Samoa and Society (EMII) and Pitcairn (EMI). The samples plot near the depleted mantle and extend towards the EMII end-member, suggesting a minor contribution from EMII to depleted mantle in their sources. (c) MgO versus $^{87}Sr/^{86}Sr(i)$ and (d) MgO versus $^{143}Nd/^{144}Nd(i)$. The field for Eocene Kamyaran mafic rocks and Late Cretaceous Mawat ophiolite from Azizi et al. (2011b) and Azizi et al. (2013), the data for Late Cretaceous Neyriz ophiolite from Shafaii Moghadam et al. (2014) and Late Cretaceous Balvard-Baft ophiolite from Shafaii Moghadam et al. (2013).

samples have lower Ti/V ratio (<20) and correlate with the arc system. In the La-Y-Nb diagram (Cabanis and Lecolle, 1989), the samples plot in the back arc, volcanic arc and MORB fields (Fig. 9b). The overlap of the island arc and MORB fields in some diagrams infers that these samples generated in the back arc region of an island arc which have HFSE and REE signatures similar to MORB or island arc basalts. On the Th/Nb versus Ce/Nb tectonic discrimination diagram, all of the samples plot in the back arc field (Fig. 9c). In addition, in the Nb versus Nb/U variation, the samples with higher Nb contents plot in the Nb enriched arc basalt (NEB) fields. The chemical compositions of the NEB were reported by Sajona et al. (1994) and Wang et al. (2013). The samples with lower Nb contents extended to the island arc to back arc fields (Fig. 9d).

Saunders and Tarney (1984), Fan et al. (2010) and Li et al. (2013) suggested that the back arc basalts can be geochemical transitional from arc or calc alkaline basalts to NMORB, and that the geochemical characteristics depend on the stage of progress of the volcanics in the back arc. Thus the early stage basalts show arc-like patterns, while later stage basalts show NMORB-like patterns that are characteristic of back arc basins (Gribble et al., 1998; Lawton and McMillan, 1999; Rolland et al., 2002; Pearce and Stern, 2006). Intra-continental BABBs with continental basement usually have EMORB-like elemental compositions (Hickey-Vargas et al., 1995; Shinjo et al., 1999), whereas intra-oceanic BABBs have geochemical features from NMORB signatures (Hawkins, 1995; Hickey-Vargas et al., 1995). Based on these characteristics, most of the basalt samples and some gabbro samples with EMORB like signatures in the Harsin-Noorabad area were generated in an intra-continental back arc like basin that formed by extension within the continental lithosphere (Figs. 7 b, 9). In contrast, some Harsin-Noorabad samples with similar REE patterns to the Mariana trough BABBs (Fig. 7b) were generated in an intra-oceanic back arc like basin (Pearce et al., 1995; Gribble et al., 1998; Tian et al., 2008; Rolland et al., 2009).

Nevertheless it remains unclear whether the Harsin-Noorabad back arc basin developed in an intraoceanic arc or an intracontinental arc domain. Based on the geochemistry features, the Harsin-Noorabad samples with EMORB and arc features formed in the earlier stage of back arc rifting at the continental margins, comparable to the Okinawa trough BABB in the present day (Shinjo et al., 1999; Shinjo and Kato, 2000; Ishizuka et al., 2002; Chen et al., 2015). The gabbro and basalt bodies with NMORB and arc characteristics formed in the later stage of the back arc basin spreading analogous to present day Mariana trough BABB (Gribble et al., 1996, 1998; Pearce et al., 2005; Chen et al., 2015). This geochemical affinity supports the development of an incipient to mature back arc basin in the Harsin-Noorabad area.

A back arc setting is closely linked to plate subduction process, and this makes back arc basin magmatism chemically and physically more variable than magmatism generated at middle oceanic ridges (Li et al., 2013). During the subduction processes, elements such as Th, Nd, Nb and Y are immobile and reflect sediment- (Nd, Nb) and slab- (Y) derived melts, whereas the Pb component is mainly controlled by fluids (Brenan et al., 1995a,b; Elliott et al., 1997; Kogiso et al., 1997; Castillo et al., 2002, 2007; Castillo, 2008). The Th/Nd versus $\varepsilon Nd(t)$ diagram (Fig. 10a) indicates a metasomatized mantle source mixed with an additional slab-derived fluid component for all samples. The involvement of slab-derived fluid is confirmed by the greater enrichment in the LILEs than the high field strength elements (HFSEs) of these rocks at shallow depths because Rb, Ba, K, Sr and Pb are mobile at low temperatures (shallow depths) causing the relatively high Ba/Th ratio of both groups (Fig. 10b). The high Ba/Th and low Th/Nb ratios indicate the influence of low-temperature aqueous fluids derived from the dehydration of

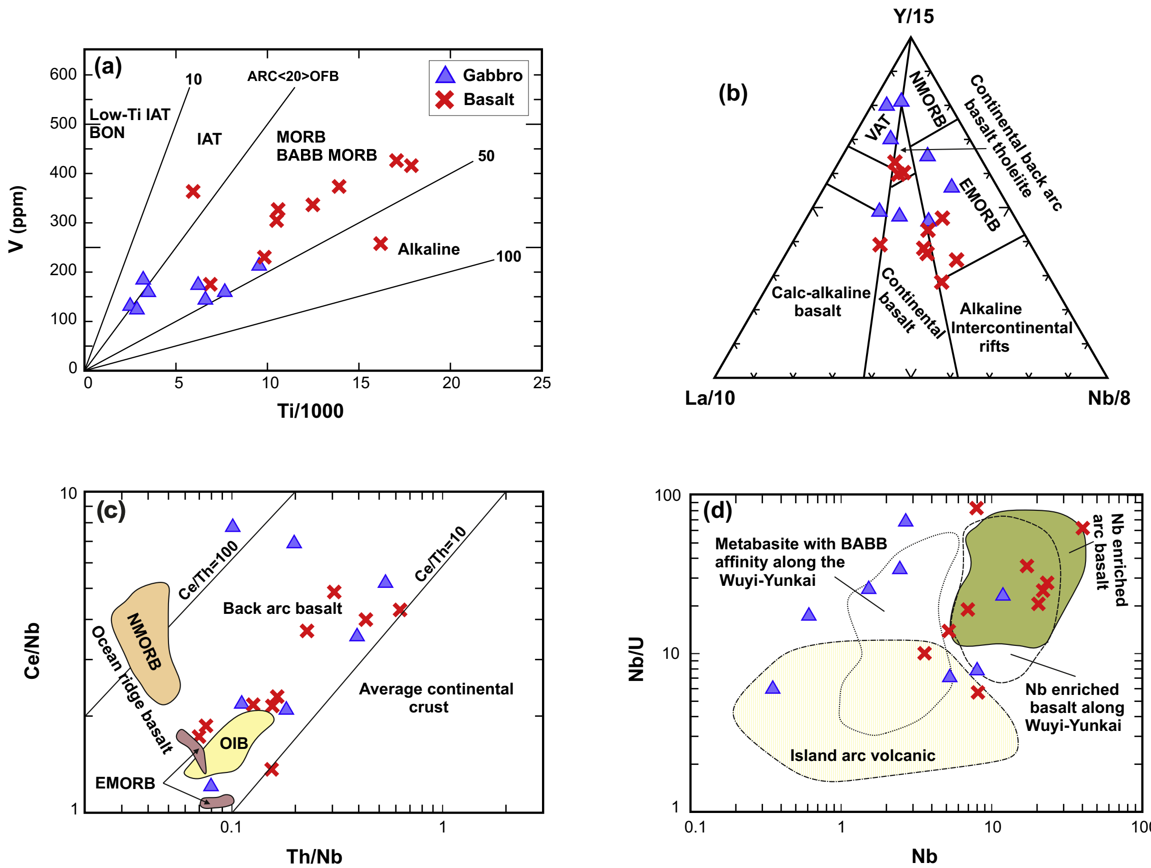

Fig. 9. (a) Ti-V discrimination diagram (Shervais, 1982) shows that the samples span in the IAT and BABB and MORB. (b) La-Y-Nb diagram (Cabanis and Lecolle, 1989). The samples span in continental back arc, volcanic arc and MORB fields. (c) Th/Nb versus Ce/Nb diagram (Sandeman et al., 2006), fields are from Saunders et al. (1980). The samples plot in the back arc field. (d) Nb versus Nb/U diagram for Harsin-Noorabad rocks. The fields of island arc volcanics and Nb enriched arc basalt are from Defant et al. (1991), Kepezhinaskas et al. (1996) and Sajona et al. (1994, 1996). The data for earliest Neoproterozoic metabasite with geochemical affinity to back arc basin and Nb enriched arc basalt from Wuyi-Yunkai domain are from Zhang et al. (2012). IAT: island arc tholeiites; MORB: middle ocean ridge basalts; BABB: back arc basin basalts; IAT: island arc tholeiite, VAT: volcanic arc tholeiite.

altered oceanic crust or dewatering of sediments (Tian et al., 2008; Li et al., 2013). In addition, the lower Ba/Th ratio in most of the basalts suggests a smaller contribution of fluid related to subduction metasomatism (Li et al., 2013).

The fluxing of the mantle source by aqueous fluids is the main control in degree of mantle melting (Taylor and Martinez, 2003; Kelly et al., 2006; Langmuir et al., 2006). The difference of the TiO_2 and Na_2O contents (Klein and Langmuir, 1987; Taylor and Martinez, 2003) indicates the degree of mantle melting: a large degree of partial melting generally leads to lower contents of incompatible elements such as TiO_2 and Na_2O (Gaetani and Grove, 1998; Falloon and Danyushevsky, 2000; Li et al., 2013). Large amount of aqueous fluids in the magma due to a larger amount of mantle melting lead to lower contents of Ti and subduction-immobile elements (Taylor and Martinez, 2003; Tian et al., 2008; Li et al., 2013). Based on these ideas, the Harsin-Noorabad samples with low TiO_2 contents are crystallized by a higher degree of mantle melting than the other samples. This is confirmed by the large amount of aqueous fluids in the magma and the isotope ratios with more depleted signature in some samples (Figs. 8, 9).

In the Harsin-Noorabad area, large volumes of pillow lava, breccia, peperite, tholeiitic basalt and gabbro are interbedded and mixed with Eocene sedimentary rocks. Braud (1978), Shahidi and Nazari (1997), Wrobel Daveau et al. (2010), Whitechurch et al. (2013) and Ao et al. (2016) have reported their age to be Eocene based on tectonics, U-Pb and K-Ar ages.

Based on the above-mentioned results on the mafic rocks in the Harsin-Noorabad area, our new report confirms the enrichment of LREEs and LILEs with negative Nb anomaly compared with the NMORB and some Nb enrichment of the basaltic rocks. These data show some relations of these rocks to metasomtized mantle above the subduction zones. We suggest that after the Late Cretaceous continental collision of the Arabian Plate and the BAVB (Azizi et al., 2013; Nouri et al., 2016), the extensional regime which occurred in the Eocene and oceanic rollback was responsible for upwelling of hot asthenosphere. The upwelling of hot asthenospheric mantle caused increasing geothermal gradient due to differentiation of the magma and partial melting of depleted mantle in the region. During this period, a large volume of mafic rocks with interbedded limestone and detrital sediments were developed (Braud, 1978; Shahidi and Nazari, 1997; Wrobel Daveau et al., 2010; Whitechurch et al., 2013), and the high discharge rates with a large difference in viscosity between the magma and host sediment lead to fingering of magma in the sediment (Kano, 2002).

9. Conclusions

In the Harsin-Noorabad area in western Iran, a number of Eocene mafic rocks exist which extend along the Zagros suture zone in a northwest-southeast direction. The major lithology include basalts and gabbros. The isotope and geochemical data confirm that the original magma was generated by partial melting of a

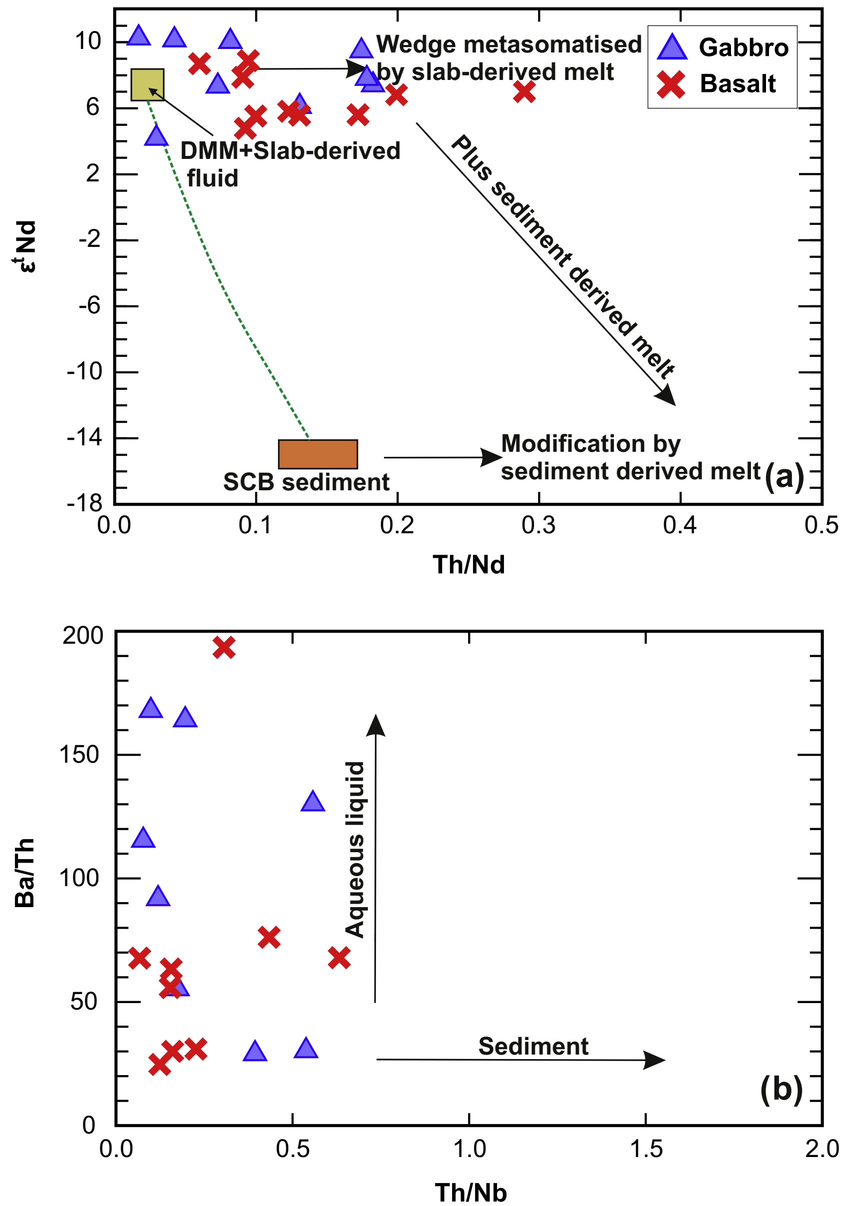

Fig. 10. (a) Th/Nd versus εNd(t) diagram. Most of the samples plot around the depleted mantle field. The variations suggest the metasomatization due to the slab-derived fluid. (b) Ba/Th versus Th/Nb diagram (Turner et al., 1997). SCB: South China block. Data sources for the composition of the end members: SCB from Wang et al. (2003), Wang et al. (2010) and Wang et al. (2011), depleted mantle and slab derived fluid from Castillo et al. (2002, 2007) and Elliott et al. (1997).

depleted lithospheric mantle and interaction with slab fluids/melts, probably in an extensional basin after the Late Cretaceous collision of the Arabian Plate and the BAVB. The production of mafic rocks at different depths, magma mixing and differentiation were responsible for the different types of Harsin-Noorabad mafic rocks.

Acknowledgments

This paper is part of F. Nouri's Ph.D. thesis and was supported by JSPS KAKENHI grant no. 25303029 in Japan. The results, including raw data and samples, are archived at University of Kurdistan (Mining Department) and Nagoya University (Department of Earth and Environmental Sciences). This version benefitted much from the critical comments of Dr. H. Shafaii Moghadam, Associate Editor and two anonymous reviewers. We also thanks to Lamiah Hashemi for checking the English language style and grammar.

References

Alavi, M., 2004. Regional stratigraphy of the Zagros fold-thrust belt of Iran and its proforeland evolution. Am. J. Sci. 304, 1–20.

Ali, S.A., Aswad, K., 2013. SHRIMP U-Pb dating of zircon inheritance in Walash arc volcanic rocks (Paleogene age), Zagros Suture Zone, NE Iraq: new insights into crustal contributions to trachytic andesite generation. Iraqi N. J. Earth Sci. 13, 45–58.

Ali, S.A., Buckman, S., Aswad, K.J., Jones, B.G., Ismail, S.A., Nutman, A.P., 2013. The tectonic evolution of a Neo-Tethyan (Eocene–Oligocene) island-arc (Walash and Naopurdan groups) in the Kurdistan region of the Northeast Iraqi Zagros Suture Zone. Isl. Arc 22, 104–125.

Allahyari, K., Saccani, E., Pourmoafi, M., Beccaluva, L., Masoudi, F., 2010. Petrology of mantle peridotites and intrusive mafic rocks from the Kermanshah ophiolitic complex (Zagros belt:Iran): implications for the geodynamic evolution of the Neo-Tethyan oceanic branch between Arabia and Iran. Ofioliti 35, 71–90.

Allahyari, K., Pourmoafi, M., Khalatbari, M., 2012. Petrology and geochemistry of the extrusive sequence of Harsin Ophiolite, W Iran. Geosci. Sci. Q. J. 84, 189–198 (in Persian).

Allahyari, K., Saccani, E., Rahimzadeh, B., Zeda, O., 2014. Mineral chemistry and petrology of highly magnessian ultramfic cumulates from the Sarve-Abad (Sawlava) ophiolites (Kurdistan, NW Iran): New evidence for boninitic

magmatism in intra-oceanic fore-arc setting in the Neo-Tethys between Arabia and Iran. J. Asian Earth Sci. 79, 312–328.
Ao, S., Xiao, W., Khalatbari-Jafari, M., Talebian, M., Chen, L., Wan, B.W.J., Zhang, Z., 2016. U-Pb zircon ages, field geology and geochemistry of the Kermanshah ophiolite (Iran): From continental rifting at 79 Ma to oceanic core complex at ca. 36 Ma in the southern Neo-Tethys. Gondwana Res. 31, 305–318.
Aswad, K.J., Al-Samman, A.H., Aziz, N.R., Koyi, A.M., 2014. The geochronology and petrogenesis of Walash volcanic rocksMawat nappes: constraints on the evolution of the northwestern Zagros suture zone, Kurdistan Region, Iraq. Arab. J. Geosci. 7, 1403–1432.
Ave Lallemant, H.G., 1976. Structure of the Canyon Mountain (Oregon) ophiolite complex and its implication for sea floor spreading. G. S. A. Spec. Pap. 173, 49.
Azizi, H., Asahara, Y., 2013. Juvenile granite in the sanandaj-Sirjan zone, NW Iran: late Jurassic–Early cretaceous arc-continent collision. Int. Geol. Rev. 55, 1523–1540.
Azizi, H., Moinevaziri, H., 2009. Review of the tectonic setting of Cretaceous to Quaternary volcanism in northwestern Iran. J. Geodyn. 47, 167–179.
Azizi, H., Asahara, Y., Mehrabi, B., Chung, S.L., 2011a. Geochronological and geochemical constraints on the petrogenesis of high-K granite from the Suffi abad areaSanandaj-Sirjan Zone, NW Iran. Chemie der Erde-Geochem. 71, 363–376.
Azizi, H., Tanaka, T., Asahara, Y., Chung, S.L., Zarrinkoub, M.H., 2011b. Discrimination of the age and tectonic setting for magmatic rocks along the Zagros thrust zone, northwest Iran, using the zircon U-Pb age and Sr-Nd isotopes. J. Geodyn. 52, 304–320.
Azizi, H., Hadi, A., Asahara, Y., Mohammad, Y.O., 2013. Geochemistry and geodynamics of the Mawat mafic complex in the Zagros suture zone northeast Iraq. Cent. Eur. J. Geosci. 5, 523–537.
Azizi, H., Najari, M., Asahara, Y., Catlos, E., Shimizu, M., Yamamoto, K., 2015a. U-Pb zircon ages and geochemistry of Kangareh and Taghiabad mafic bodies in northern Sanandaj-Sirjan Zone, Iran: evidence for intra-oceanic arc and back-arc tectonic regime in Late Jurassic. Tectonophysics 660, 47–64.
Azizi, H., Zanjefili Beiranvand, M., Asahara, Y., 2015b. Zircon U–Pb ages and petrogenesis of a tonalite–trondhjemite–granodiorite (TTG) complex in the northern Sanandaj–Sirjan Zone, northwest Iran: evidence for Late Jurassic arc–continent collision. Lithos 216-217, 178–195.
Azizi, H., Mohammadi, K., Asahara, Y., Tsuboi, M., Daneshvar, N., Mehrabi, B., 2016. Strongly peraluminous leucogranite (Ebrahim-Attar granite) as evidence for extensional tectonic regime in the Cretaceous, Sanandaj Sirjan zone, northwest Iran. Chemie der Erde-Geochem. 76, 529–541.
Braud, J., 1978. Geology Map of Kermanshah, Scale 1:250000.NO. C6. Geol. Surv., Iran.
Brenan, J.M., Shaw, H.F., Ryerson, F., 1995a. Experimental evidence for the origin of lead enrichment in convergent-margin magmas. Nature 378, 54–56.
Brenan, J.M., Shaw, H.F., Ryerson, F.J., Phinney, D.L., 1995b. Mineral-aqueous fluid partitioning of trace elements at 900 °C and 2.0 G Pa: constraints on the trace element chemistry of mantle and deep crustal fluids. G. C. A. 59, 3331–3350.
Buday, T., 1980. The Regional Geology of Iraq: Stratigraphy and Paleogeography. State Organization, pp. 1.
Cabanis, B., Lecolle, M., 1989. Le diagramme La/10–Y/15–Nb/8: un outil pour la discrimination des series volcaniques et la mise en evidence des processus demelange et/ou de contamination crustale. Comtes Rendus de l'Académie desScience Ser. II 309, 2023–2029.
Castillo, P.R., Solidum, R.U., Punogbayan, R.S., 2002. Origin of high field strength element enrichment in the Sulu Arc, southern Philippines, revisited. Geology 30, 707–710.
Castillo, P.R., Rigby, S.J., Solidum, R.U., 2007. Origin of high field strength element enrichment in volcanic arcs: geochemical evidence from the southern Sulu Arc, southern Philippines. Lithos 97, 271–288.
Castillo, P.R., 2008. Origin of the adakite-high-Nb basalt association and its implications for post-subduction magmatism in Baja California, Mexico. Geol. Soc. Am. Bull. 120, 451–462.
Chen, S.S., Shi, R.D., Zou, H.B., Huang, Q.S., Liu, D.L., Gong, X.H., Yi, G.D., Wu, K., 2015. Late Triassic island-arc-back-arc basin development along the Bangong-Nujiang suture zone (central Tibet): Geological, geochemical and chronological evidence from volcanic rocks. Lithos 230, 30–45.
Coleman, R.G., Donato, M.M., 1979. Oceanic plagiogranite revisited. In Trondhjemites:dacites and related rocks, vol. 6. Elsevier, Amsterdam, pp. 149–168.
DePaolo, D.J., Wasserburg, G.J., 1976. Nd isotopic variations and petrogenetic models. Geophys. Res. Lett. 3, 249–252.
Deer, W.A., Howie, R.A., Zussman, J., 1991. An Introduction to the Rock Forming Mineral. Longman, London.
Defant, M.J., Richerson, P.M., de Boer, J.Z., Stewart, R.H., Maury, R.C., Bellon, H., Jackson, T.E., Restrepo, J.F., 1991. Andesite and dacite genesis via contrasting processes: the geology and geochemistry of E1 Valle volcano, Panama. Contrib. Mineral. Petrol. 106, 309–324.
Delaloye, M., Desmons, J., 1980. Ophiolites and mélange terranes in Iran: a geochronological study and its paleotectonic implications. Tectonophysics 68, 83–111.
Desmons, J., Beccaluva, L., 1983. Mid-oceanic ridge and island arc affinities in ophiolites from Iran:Paleogeographic implication. Chem. Geol. 39, 39–63.
Elliott, T., Plank, T., Zindler, A., White, W., Bourdon, B., 1997. Element transport from slab to volcanic front at the Mariana arc. J. Geophys. Res. 102, 14991–15019.
Falloon, T.J., Danyushevsky, L.V., 2000. Melting of refractory mantle at 1.5, 2 and 2.5 GPa under anhydrous and H2O-undersaturated conditions: implications for the petrogenesis of high-Ca boninites and the influence of subduction components on mantle melting. J. Petrol. 41, 257–283.
Fan, W., Wang, Y., Zhang, A., Zhang, F., Zhang, Y., 2010. Permian arc-back-arc basin development along the Ailaoshan tectonic zone: geochemical, isotopic and geochronological evidence from the Mojiang volcanic rocks, Southwest China. Lithos 119, 553–568.
Gaetani, G.A., Grove, T.L., 1998. The influence of water on melting of mantle peridotite. Contrib. Mineral. Petrol. 131, 323–346.
Gerlach, D.C., Ave Lallemant, H.G., Leeman, W.P., 1981. An island arc origin for the Canyon Mountain ophiolite complexeastern Oregon, USA. Earth Planet. Sci. Lett. 53, 255–265.
Ghazi, A.M., Hassanipak, A.A., 1999. Geochemistry of subalkaline and alkaline extrusive from the Kermanshah ophiolite, Zagros Suture Zone, Western Iran: implications for Tethyan plate tectonics. J. Asian Earth Sci. 17, 319–332.
Greenough, J.D., Dostal, J., Mallory-Greenough, L.M., 2005. Igneous rock associations 5. Oceanic island volcanism II: mantle processes. Geosci. Can. 32.
Gribble, R.F., Stern, R.J., Bloomer, S.H., Stuben, D., O'Hearn, T., Newman, S., 1996. MORB mantle and subduction components interact to generate basalts in the southern Mariana Trough back-arc basin. G. C. A. 60, 2153–2166.
Gribble, R.F., Stern, R.J., Newman, S., Bloomer, S.H., O'Hearn, T., 1998. Chemical and isotopic composition of lavas from the northern Mariana Trough: implications for magma genesis in back-arc basins. J. Petrol. 39, 125–154.
Hawkins, J.W., 1995. The geology of the Lau Basin. In: Taylor, B. (Ed.), Back-arc Basins: Tectonics and Magmatism. Plenum Press, New York, pp. 63–138.
Hickey-Vargas, R., Hergt, J.M., Spadea, P., 1995. The Indian Ocean-type isotopic signature in western Pacific marginal basins: origin and signatures. In: Taylor, B., Natland, J. (Eds.), Active Margins and Marginal Basins of the Western Pacific, Geophysical Monograph 88. , pp. 175–197, Washington, DC.
Ishizuka, O., Yuasa, M., Uto, K., 2002. Evidence of porphyry copper-type hydrothermal activity from a submerged remnant back-arc volcano of the Izu-Bonin arc: implications for the volcano tectonic history of back-arc seamounts. Earth Planet. Sci. Lett. 198, 381–399.
Jahn, B.M., Wu, F., Lo, C.H., Tsai, C.H., 1999. Crust-mantle interaction induced by deep subduction of the continental crust: geochemical and Sr-Nd isotopic evidence from post-collisional mafic-ultramafic intrusions of the northern Dabie complex, central China. Chem. Geol. 157, 119–146.
Jassim, S.Z., Goff, J., 2006. Geology of Iraq. Dolin, Prague and Moravian Museum, Burno, pp. 32–44.
Kano, K., 2002. Middle Miocene volcaniclastic dikes at Kukedo, Shimane Peninsula, and SW Japan: fluidization of volcaniclastic beds by emplacement of syn-volcanic andesitic dikes. In: Skilling, I.P., White, J.D.L., McPhie, J. (Eds.), Peperite: Processes and Products of Magma-Sediment Mingling. J. Volcan. Geotherm. Res. 114, 81–94.
Karimi Bavandpur, A., Hajihoseini, A., 1999. Geological Map of Kermanshah. NO. 5458. Geol. Surv., Iran.
Kazmin, V.G., Ricou, L.F., Sbortshikov, I.M., 1986. Structure and evolution of the passive margin of the eastern Tethys. Tectonophysics 123, 153–179.
Kelly, K.A., Plank, T., Grove, T.L., Stolper, E.M., Newman, S., Hauri, E., 2006. Man-tle melting as a function of water content beneath back-arc basins. J. Geophys. Res., 111, http://dx.doi.org/10.1029/2005JB003732 B09208.
Kepezhinaskas, P.K., Defant, M.J., Drummond, M.S., 1996. Progressive enrichment of island–arc mantle by melt–peridotite interaction from Kamchatka adakites. G. C. A. 60, 217–1229.
Kiani, M., Ahmadi-Khalaji, A., Kamali, Z., Moghadam, H.S., 2015. Geochemistry of diabasic dikes and andesitic-basaltic lavas in Noorabad-Kermanshah ophiolite. J. Tethys 3, 001–015.
Klein, E.M., Langmuir, C.H., 1987. Global correlations of ocean ridge basalt chemistry with axial depth and crustal thickness. J. Geophys. Res. 92, 8089–8115.
Kogiso, T., Tatsumi, Y., Nakano, S., 1997. Trace element transport during dehydration processes in the subducted oceanic crust: 1. Experiments and implications for the origin of ocean island basalts. Earth Planet. Sci. Lett. 148, 193–205.
Langmuir, C.H., Bézos, A., Escrig, S., Parman, S.W., 2006. Chemical systematics andhydrous melting of the mantle in back-arc basins. In: Christie, D.M., et, al. (Eds.), Back-arc Spreading Systems: Geological, Biological, Chemical and Physical Inter-actions. Geophysical Monograph Series, vol. 166. American Geophysical Union, pp. 87–146.
Lawton, T.F., McMillan, N.J., 1999. Arc abandonment as a cause for passive continental rifting: comparison of the Jurassic Mexican Borderland rift and the Cenozoic Rio Grande rift. Geology 27, 779–782.
LeBas, M.J., Le Maitre, R.W., Streckeisen, A., Zanettin, B., 1986. A chemical classification of volcanic rocks based on the total alkali silica diagram. J. Petrol. 27, 745–750.
Li, L., Lin, S., Xing, G., Davis, D.W., Davis, W.J., Xiao, W., Yin, C., 2013. Geochronology and geochemistry of volcanic rocks from the Shaojiwa Formation and Xingzi Group, Lushan area, SE China: implications for Neoproterozoic back-arc basin in the Yangtze Block. Precambrian Res. 238, 1–17.
Menzies, M., Blanchard, D., Xenophontos, C., 1980. Genesis of the Smart Ville arc ophioliteSierra Nevada foothills, California. Am J. Sci. 180, 329–344.
Miyashiro, A., 1973. The Troodos ophiolitic complex was probably formed in an island arc. Earth Planet. Sci. Lett. 19, 128–224.

Mohajjel, M., Fergusson, C.L., Sahandi, M.R., 2003. Cretaceous-Tertiary convergence and continental collision, Sanandaj-Sirjan Zone, western Iran. J. Asian Earth Sci. 21, 397–412.
Monod, O., Kozlu, H., Ghienne, J.F., Dean, W.T., Gunat, Y., Herisse, A.L., Paris, F., Robardet, M., 2003. Late ordovician glaciation in southern Turkey. Terra Nova 15, 249257.
Morimoto, N., 1988. The nomenclature of pyroxenes. Min. Mag. 52, 1123–1133.
Nouri, F., Azizi, H., Golonka, J., Asahara, Y., Orihashi, Y., Yamamoto, K., Tsuboi, M., Anma, R., 2016. Age and petrogenesis of Na-rich felsic rocks in western Iran: evidence for closure of the southern branch of the Neo-Tethys in the Late Cretaceous. Tectonophysics 671, 151–172.
Okay, A.I., Tüysüz, O., 1999. Tethyan sutures of northern Turkey. Geol. Soc. Lond. Spec. Pub. J. 156, 475–515.
Okay, A.I., Monod, O., Monie, P., 2002. Triassic blueschists and eclogites from northwest Turkey: vestiges of the Paleo Tethyan subduction. Lithos 64, 155–178.
Okay, A.I., Bozkurt, E., Satir, M., Yigitbas, E., Crowley, Q.G., Shang, C.K., 2008. Defining the margin of Avalonia in the Pontides: geochronological data from the late Proterozoic and Ordovician granitoids from NW Turkey. Tectonophysics 461, 252–264.
Okay, A.I., 2008. Geology of Turkey: a synopsis. Anschnitt 21, 19–42.
Paul, A., Hatzfeld, D., Kaviani, A., Tatar, M., Péquegnat, C., 2010. Seismic imaging of the lithospheric structure of the Zagros mountain belt (Iran). Geol. Soc. Lond Spec. Pub. 330, 5–18.
Pearce, J.A., Stern, R.J., 2006. The origin of back-arc basin magmas: trace element and isotope perspectives. In: Christie, D.M., Fisher, C.R., Lee, S.M., Givens, S. (Eds.), Back-Arc Spreading Systems: Geological, Biological, Chemical and Physical Interactions. Am. Geophys. Union Geophys. Monograph 166, 63–86.
Pearce, T.H., Gorman, B.E., Birkett, T.C., 1977. The relationship between major element chemistry and tectonic environment of basic and intermediate volcanic rocks. Earth Planet. Sci. Lett. 36, 121–132.
Pearce, J.A., Baker, P.E., Harvey, P.K., Luff, I.W., 1995. Geochemical evidence for subduction fluxes, mantle melting and fractional crystallization beneath the South Sandwich island arc. J. Petrol. 36, 1073–1109.
Pearce, J.A., Stern, R.J., Bloomer, S.H., Fryer, P., 2005. Geochemical mapping of the Mariana arc-basin system: implications for the nature and distribution of subduction components. Geochem. Geophys. Geosyst. 6, Q07006.
Pearce, J.A., 2008. Geochemical fingerprinting of oceanic basalts with applications to ophiolite classification and the search for Archaean oceanic crust. Lithos 100, 14–48.
Peccerillo, A., Taylor, S.R., 1976. Geochemistry of Eocene calc-alkaline volcanic rocks from the Kastamonu area, northern Turkey. Contrib. Mineral. Petrol. 58, 63–81.
Pillevuit, A., Marcoux, J., Stampfli, G., Baud, A., 1997. The Oman exotics: a key to understanding of the Neotethyan geodynamic evolution. Geodin. Acta 10, 209–238.
Reagan, M.K., Ishizuka, O., Stern, R.J., Kelley, K.A., Ohara, Y., Blichert-Toft, J., Bloomer, S.H., Cash, J., Fryer, P., Hanan, B.B., Hickey-Vergas, R., Ishii, T., Kimura, J.I., Peate, D.W., Rowe, M.C., Woods, M., 2010. Fore-arc basalts and subduction initiation in the Izu-Bonin Mariana system. Geochem. Geophys. Geosyst. 11, 1–17.
Ricou, L.E., Braud, J., Brunn, J.A., 1977. Le Zagros. Meímoire Societe Geíologique de France. Hors-Seírie 8, 33–52.
Rolland, Y., Picard, C., Pecher, A., Lapierre, H., Bosch, D., Keller, F., 2002. The cretaceous Ladakh arc of NW Himalaya-slab melting and melt-mantle interaction during fast northward drift of Indian Plate. Chem. Geol. 182, 139–178.
Rolland, Y., Galoyan, G., Bosch, D., Sosson, M., Corsini, M., Fornari, M., Verati, C., 2009. Jurassic back-arc and Cretaceous hot-spot series in the Armenian ophiolites: implications for the obduction process. Lithos 112, 163–187.
Şengör, A.M.C., Yilmaz, Y., 1981. Tethyan evolution of Turkey:A plate tectonic approach. Tectonophysics 75, 181–241.
Şengör, A.M.C., 1987. Tectonics of the Tethys sides: orogenic collage development in a collisional setting. Ann. Rev. Earth Planet. Sci. 15, 213–244.
Saccani, E., Allahyari, K., Beccaluva, L., Bianchini, G., 2013. Geochemistry and petrology of the Kermanshah ophiolites (Iran): implication for the interaction between passive riftingoceanic accretion, and OIB-type components in the Southern Neo-Tethys Ocean. Gondwana Res. 24, 392–411.
Saccani, E., Allahyari, K., Rahimzadeh, B., 2014. Petrology and geochemistry of mafic magmatic rocks from the Sarve-Abad ophiolites (Kurdistan region, Iran): evidence for interaction between MORB-type asthenosphere and OIB-type components in the southern Neo-Tethys Ocean. Tectonophysics 621, 132–147.
Sajona, F.G., Bellon, H., Maury, R.C., Pubellier, M., Cotton, J., Rangin, C., 1994. Magmatic response to abrupt changes in tectonic setting: pliocene–Quaternary calc-alkaline lavas and Nb-enriched basalts of Leyte and Mindanao (Philippines). Tectonophysics 237, 47–72.
Sajona, F.G., Maury, R.C., Bellon, H., Cotton, J., Defant, M.J., 1996. High field strength element enrichment of Pliocene-Pleistocene island arc basalts, Zamboanga Peninsula, Western Mindanao (Philippines). J. Petrol. 37, 693–726.
Sandeman, H.A., Hanmer, S., Tella, S., Armitage, A.A., Davis, W.J., Ryand, J.J., 2006. Petrogenesis of Neoarchaean volcanic rocks of the MacQuoid supracrustal belt:a back-arc setting for the northwestern Hearne subdomain, western Churchill Province, Canada. Precambrian Res 144 (1/2), 126–139.
Saunders, A.D., Tarney, J., 1984. Geochemical characteristics of basaltic volcanism within back-arc basins. Geol. Soc. Lond. Spec. Pub. 16, 59–76.
Saunders, A.D., Tarney, J., Marsh, N.G., Wood, D.A., 1980. Ophiolites as an ocean crust or marginal basin crust: a geochemical approach. In: Panayiotou, A. (Ed.), Ophiolites. Proc. Internat. Ophiolite Symp. Geol. Surv. Dept. Cyprus Nicosia. , pp. 193–204.
Shafaii Moghadam, H., Stern, R.J., 2011. Geodynamic evolution of Upper Cretaceous Zagros ophiolites: formation of oceanic lithosphere above a nascent subduction zone. Geol. Mag. 148, 762–801.
Shafaii Moghadam, H., Stern, R., 2015. Ophiolites of Iran: keys to understanding the tectonic evolution of SW Asia: (II) Mesozoic ophiolites. J. Asian Earth Sci. 100, 31–56.
Shafaii Moghadam, H., Rahgoshay, M., Banitaba, A., 2009. Geochemistry and petrogenesis of basaltic flows in the Nain–Dehshir ophiolites. Iran. Soc. Crystal. Min. 16, 603–612.
Shafaii Moghadam, H., Stern, R.J., Chiaradia, M., Rahgoshay, M., 2013. Geochemistry and tectonic evolution of the Late Cretaceous Gugher-Baft ophiolite, central Iran. Lithos 168 (168–169), 33–47.
Shafaii Moghadam, H., Zaki Khedr, M., Chiaradia, M., Stern, R.J., Bakhshizad, F., Arai, S., Ottley, C.J., Tamura, A., 2014. Supra-subduction zone magmatism of the Neyriz ophiolite, Iran: constraints from geochemistry and Sr-Nd-Pb isotopes. Int. Geol. Rev. 56 (11), 1395–1412.
Shahidi, A., Nazari, H., 1997. Geological Map of Harsin. NO. 5558. Geol. Surv., Iran.
Shen, X.M., Zhang, H.X., Wang, Q., Ma, L., Yang, Y.H., 2014. Early Silurian (~440Ma) adakitic, andesitic and Nb-enriched basaltic lavas in the southern Altay Range, Northern Xinjiang (western China): Slab melting and implications for crustal growth in the Central Asian Orogenic Belt. Lithos 206, 234–251.
Shervais, J.W., 1982. Ti-V plots and the petrogenesis of modern and ophiolite lavas. Earth Planet. Sci. Lett. 59, 101–118.
Shinjo, R., Kato, Y., 2000. Geochemical constraints on the origin of bimodal magmatism at the Okinawa Trough, an incipient back-arc basin. Lithos 54, 117–137.
Shinjo, R., Chung, S.L., Kato, Y., Kimura, M., 1999. Geochemical and Sr–Nd isotopic characteristics of volcanic rocks from the Okinawa Trough and Ryukyu Arc: implications for the evolution of a young, intracontinental back arc basin. J. Geophys. Res. 104, 10591–10608.
Stöcklin, J., Nabavi, M.H., 1972. 1/2,500,000 Sheet, Tectonic Map of Iran. Geol. Surv., Iran.
Stracke, A., Bizimis, M., Salters, V.J., 2003. Recycling oceanic crust: quantitative constraints. Geochem. Geophys. Geosyst. 4 (3), 8003–10.1029/GC0223.
Sun, S.S., McDonough, W.F., 1989. Chemical and isotopic systematic of oceanic basalts: implication for mantle composition and processes. In: Sunders, A.D., Norry, M.J., (Eds.), Magmatic in Oceanic Basins. Geol. Soc. Lond. Spec. Pub. 42, 313–345.
Tahmasbi, Z., Kiani, M., Khalaji, A.A., 2016. Petrology and geochemistry of diabasic dikes and andesitic-basaltic lavas in Noorabad-Harsin ophiolite, SE of Kermanshah, Iran. J. Earth Sci. 27, 935–944.
Tanaka, T., Togashi, S., Kamioka, H., Amakawa, H., Kagami, H., Hamamoto, T., Yuhara, M., et al., 2000. JNdi-1: a neodymium isotopic reference in consistency with LaJolla neodymium. Chem. Geol. 168, 279–281.
Taylor, B., Martinez, F., 2003. Back-arc basin basalt systematics. Earth Planet. Sci. Lett. 210, 481–497.
Tian, L.Y., Castillo, P.R., Hawkins, J.W., Hilton, D.R., Hanan, B.B., Pietruszka, A.J., 2008. Major and trace element and Sr–Nd isotope signatures of lavas from the Central au Basin: implications for the nature and influence of subduction components in the back-arc mantle. J. Volcan. Geotherm. Res. 178, 657–670.
Turner, S., Hawkesworth, C., Rogers, N., Bartlett, J., Worthington, T., Hergt, J., Pearce, J., Smith, I., 1997. 238U-230Th disequilibria, magma petrogenesis, and flux rates beneath the depleted Tonga-Kermadec island arc. G. C. A. 61, 4855–4884.
Vergés, J., Saura, E., Casciello, E., Fernàndez, M., Villaseñor, A., Jiménez-Munt, I., García-Castellanos, D., 2011. Crustal-scale cross-sections across the NW Zagros belt: implications for the Arabian margin reconstruction. Geol. Mag. 148, 739–776.
Verma, S.P., Guevara, M., Agrawal, S., 2006. Discriminating four tectonic settings: five new geochemical diagrams for basic and ultrabasic volcanic rocks based on log–ratio transformation of major-element data. J. Earth Syst. Sci. 115, 485–528.
Wang, Y.J., Fan, W.M., Guo, F., Peng, T.P., Li, C.W., 2003. Geochemistry of Mesozoic mafic rocks around the Chenzhou–Linwu fault in South China: implication for the lithospheric boundary between the Yangtze and the Cathaysia Blocks. Int. Geol. Rev. 45, 263–286.
Wang, Y.J., Zhang, F.F., Fan, W.M., Zhang, G.W., Chen, S.Y., Cawood, P.A., Zhang, A.M., 2010. Tectonic setting of the South China Block in the early Paleozoic: resolving intracontinental and ocean closure models from detrital zircon U–Pb geochronology. Tectonics 29, TC6020, http://dx.doi.org/10.1029/2010TC002750.
Wang, Y.J., Zhang, A.M., Fan, W.M., Zhao, G.C., Zhang, G.W., Zhang, F.F., Zhang, Y.Z., Li, S.Z., 2011. Kwangsian crustal anatexis within the eastern South China Block: geochemical, zircon U-Pb geochronological and Hf isotopic fingerprints from the gneissoid granites of Wugong and Wuyi-Yunkai Domains. Lithos 127, 239–260.
Wang, Y., Zhang, A., Fan, W., Zhang, Y., Zhang, Y., 2013. Origin of paleo subduction-modified mantle for Silurian gabbro in the Cathaysia Block: geochronological and geochemical evidence. Lithos 160, 37–54.
Weaver, B.L., 1991. The origin of ocean island basalt end-member compositions: trace element and isotopic constraints. Earth Planet. Sci. Lett. 104, 381–397.

Whattam, S.A., Stern, R.J., 2011. The subduction initiation rule: a key for linking ophiolites, intra-oceanic forearcs, and subduction initiation. Contrib. Mineral. Petrol. 162, 1031–1045.

Whitechurch, H., Omrani, J., Agard, P., Humbert, F., Montigny, R., Jolivet, L., 2013. Evidence for Paleocene-Eocene evolution of the foot of the Eurasian margin (Kermanshah ophiolite, SW Iran) from back-arc to arc: implications for regional geodynamics and obduction. Lithos 182–183, 11–32.

Wrobel Daveau, J.C., Ringenbach, J.C., Tavakoli, S., Ruiz, G., Masse, P., Frizonde Lamotte, D., 2010. Evidence for mantle exhumation along the Arabian margin in the Zagros (Kermanshah area, Iran). Arab. J. Geosci. 3, 499–513.

Yilmaz, H., Özel, S., 2008. Crustal structure of the eastern part of Central Anatolia (Turkey). Turkey.J. Earth Sci. 17, 169–185.

Zhang, A.M., Wang, Y.J., Fan, W.M., Zhang, Y.Z., Yang, J., 2012. Earliest Neoproterozoic (ca. 1. 0 Ga) arc–back-arc basin nature along the northern Yunkai Domain of the Cathaysia Block: geochronological and geochemical evidence from the metabasite. Precambrian Res. 220–221, 217–233.